



university of
 groningen

UNIVERSITY OF GRONINGEN

MASTER THESIS

Dust rings in TW Hya

Author:
Manou IJTSMA

Supervisor:
Prof. Dr. I.E.E. KAMP

*A thesis submitted in fulfillment of the requirements
for the degree of Master of science*

February 13, 2019

Abstract

Manou IJT SMA

Dust rings in TW Hya

Recent high spatial resolution ALMA observations show a ringed substructure in the protoplanetary disk of the nearby T Tauri star TW Hya. With the help of a thermo-chemical disk code called ProDiMo which calculates both, the continuum radiative transfer and the gas thermal balance/chemistry, the influence of this substructure on the gas will be investigated. The starting point for this thesis is an existing protoplanetary disk model from the DIANA project which has a smooth surface density and hence also surface brightness profile. Modifications of this model will be made to match the model as good as possible to the observed surface brightness profile. From the final run it could be concluded that the disk mass went down by 34 %. The substructure of the rings has caused the dust temperature in the outer regions of the disk to increase. The gas temperatures did not show a big deviation, but the CO iceline was shifted resulting in an increase of the CO ice mass of $8.5 \times 10^{-8} M_{\text{sun}}$. The smallest change in line fluxes between the original model and the DIANA model is $F_{\text{line}} = 1.36 \times 10^{-21} \text{W/m}^2$, which should be detectable by ALMA.

The final model is also compared to an existing disk model of TW Hya by van Boekel et al. (2017) which matches the gas surface density within a factor two, but the surface density of the large grains with sizes 1-10 mm differs by a factor 30. The reason for this difference is not found as the van Boekel et al. (2017) paper gives to little insight in the modeling method used to obtain this profile.

Acknowledgements

This thesis could not be completed without the help of some. Therefore I would like to thank two persons for their help and expertise.

First, I would like to thank my thesis supervisor, Prof. Dr. Inga Kamp, for her guidance. I would also like to thank her for her positivity which has kept me motivated to keep working on the thesis even if the things are not going as expected.

Second, I would like to thank Dr. Christian Rab for helping me with the installation of the python adaption of the model and creating a new surface brightness profile for me to use. I also would like to thank him for helping out with the computational issues that arose during this thesis.

With their help and expertise I feel this thesis is the best version of itself.

Contents

Abstract	iii
Acknowledgements	v
1 Introduction	1
1.1 Stars and protoplanetary disks	1
1.2 Planets forming in disks	2
1.3 Modeling the disks and host stars	3
1.4 TW Hya	3
1.5 Surface brightness	4
1.6 Surface density	5
1.7 Chemistry	8
1.8 Aim	8
2 The model	9
2.1 Data visualization with ProDiMopy	9
2.2 The DIANA project	10
2.3 Initial model parameters	11
3 Method	13
3.1 Surface brightness	13
3.1.1 Determining the model surface brightness	14
3.1.2 Adapting the model	15
3.1.3 Calculating $f_{I/M}$	15
3.1.4 Manipulating the column density	17
3.2 Surface density	17
3.3 Chemistry	19
4 Results	21
4.1 Surface brightness	21
4.1.1 First run	21
4.1.2 High resolution	22
4.1.3 Background	23
4.1.4 Final model	27
4.2 Surface density	29
4.3 Chemistry	30
5 Discussion	35
6 Conclusion	37
Bibliography	39

Chapter 1

Introduction

Mankind has always wondered about the possible existence of other planets such as our own earth outside the solar system. In 1995 the first extra solar planet has been discovered: a Jupiter-mass companion to the star 51 Pegasi. Its existence was derived from the periodic variations in the star's radial velocity (Mayor and Queloz, 1995). This companion lies only about eight million kilometres from the star, which would be well inside the orbit of Mercury in the Solar System. Mayor and Queloz (1995) argue that this object might be a gas-giant planet that has migrated to this location through orbital evolution, or from the radiative stripping of a brown dwarf. The theory explaining how planets should form existed well before this discovery, however this type of planet did not fit those theories. Hence the theory was revised and migration was included as a firm part of the model for planet formation. Currently, the protoplanetary disks around young stars are thought to be the formation site of planets. Recent ALMA and SPHERE observations have shown substructure in these protoplanetary disks which could be related to the planet formation process.

1.1 Stars and protoplanetary disks

The extra-solar planets show a wide range of diversity in orbital parameters, distances to their main star and chemical compositions. This wide range of differences is linked to the range of properties of their birth places: the disk like structures around young stars composed of gas and dust particles. These disks share many of the properties of the solar nebula from which the Sun and our planetary system formed, although their masses, radial dimensions and internal structures can be very different (Williams and Cieza, 2011). The protoplanetary disks are formed along with their host star through the gravitational collapse of their parent cloud and can thus be considered a byproduct of star formation. There are a number of competing theories to explain how the collapse of a cloud to a star exactly works. One of these theories is the inside-out collapse model (Shu, 1977).

In this inside-out collapse model it is assumed that the parent cloud is in hydrostatic equilibrium for some time before the collapse itself starts. Another assumption made is that the parent cloud rotates as a solid body and that the cloud is rotating slowly such that the centrifugal force is relatively small compared to the gravity and pressure of the cloud. Then, the early stages of collapse are almost radial. In this limit, we can distinguish between an outer envelope which stays almost spherical and an inner region that gets distorted due to rotation and forms an equatorial accretion disk. Depending on the specific angular momentum (that is the angular momentum per unit of mass) of a gas parcel, it

will either be able to accrete onto the protostellar core (very low specific angular momentum) or accrete onto the equatorial disk at some radius corresponding to its angular momentum. A particle initially located on the rotation axis of the cloud has zero angular momentum and will simply fall directly to the center, i.e. the star. The maximum possible distance from the star at which such a gas parcel can end up is called the centrifugal radius r_c , and it is reached by particles that are initially located in the midplane of the system, i.e. the plane perpendicular to the rotation axis.

After this formation stage, also called the class 0 stage, the disk continues on into the second phase. In this second phase, also referred to as a class I disk, the rapid inside-out gravitational collapse of molecular cloud cores conserves angular momentum, producing a protostar surrounded by a disk and an optically thick in-falling envelope. The driving mechanism for the de-acceleration of the in-falling envelope is still debated. One of the theories suggest a strong stellar wind breaking out at the rotational poles, reversing the infall and producing bipolar outflows.

The next phase is disk dispersal. After the collapse of the cloud to form the protostar and disk system the last bits of the tenuous cloud are likely driven away by radiation pressure and also possibly winds from the young protostar. These disk winds are rather invoked to disperse the disk and not so much the cloud, thus acting more efficiently in the later evolutionary stages of the disk. These photoevaporative winds occur when high-energy radiation is incident on a disk, and its upper layers are heated to well above the midplane temperature. At sufficiently large radius (i.e., high enough in the potential well) the thermal energy of the heated layer exceeds its gravitational binding energy, and the heated gas escapes. The result is a centrifugally-launched, pressure-driven flow, which is referred to as a photoevaporative wind (Alexander et al., 2014).

This phase seems to be intimately connected with the disk formation phase in which the star and its disk become optically visible, also referred to as a class II disk. The main advantage of these class II disks is that they are more exposed systems, meaning they are more easily accessible to observations.

1.2 Planets forming in disks

In the final stages of disk evolution, where disk dispersal occurs, the disk material is removed. Mechanisms for disk clearing include accretion onto the protostar, forming planets and forming small objects.

Planets are formed in the protoplanetary disks by collisions between the dust grains. As the dust settles towards the disk mid-plane the density of grains rises, which increases the likelihood of grain-grain collisions. There are three possible outcomes of a grain-grain collision: the grains can stick, rebound or shatter. The probability of sticking depends on the relative velocity of the grains and their chemical and physical properties (Blum et al., 2006). High speed collisions are more likely to result in shattering, while low speed collisions are more likely to result in sticking. Icy and tarry grain surfaces are likely to enhance sticking. This grain growth happens in three steps: first the tiny grains stick electrostatically; then small grains grow via collisions; and finally planetesimals grow via accretion.

The timescale of this disk clearing puts constraints on the planet formation process, as a fully dispersed disk has no material left to form planets. The oldest observed (gas-rich) protostellar disks are about a few $10^6 - 10^7$ years old (Haisch, Lada, and Lada, 2001), so the

disk must be cleared within this time frame. Once the disk has dispersed, we are left with a new young hydrogen burning star, possibly surrounded by a planetary system.

Many protoplanetary disks show central cavities, rings, or spiral arms linked to low-mass stellar or planetary companions. However, few such features are conclusively tied to bodies embedded in the disks. These small features of the disk surface could even cast shadow as the starlight grazes the surface (Isella and Turner, 2018). These substructures are investigated in the Disk Substructures at High Angular Resolution Project (DSHARP). This project provides a large sample of protoplanetary disks with substructures that could be induced by young forming planets (Zhang et al., 2018).

1.3 Modeling the disks and host stars

To investigate how the chemical properties of such a star and its disk vary with physical properties and geometry the use of models is a very common practice. For these models important boundary conditions are derived from the distribution of gaseous and solid materials around the young stars. The disk models are widely used by the community to analyze and interpret line and continuum observations, such as photometric fluxes, low- and high-resolution spectroscopy, images and visibility data, from X-ray to centimeter wavelengths.

Since the use of models is such a common practice a lot of different models exist, which can be divided into two categories. First, the continuum radiative transfer models which explore the disk shape, dust temperature and grain properties. Examples of models such as these are MCFOST (Pinte et al., 2006) and MCMax (Min et al., 2009), both using a Monte-Carlo method for the radiative transfer which uses an energy diffusion approximation to improve the accuracy of the temperature structure in highly obscured regions of the disk, where photon counts are low. Second, the thermo-chemical models which usually include chemistry and UV and X-ray physics to explore the temperature and chemical properties of the gas. This approach has been mostly used to explain submm molecular data from the outer disk. However, it has been used for years now also for near- and mid-IR spectral data - Carmona et al. (2014), Hein Bertelsen et al. (2014), Woitke et al. (2018b).

1.4 TW Hya

In this thesis the protoplanetary disk of TW Hya will be modeled. TW Hya, or TW Hydrae as it is also called, is a T Tauri type of star. The T Tauri stars are very young stars with an age of less than 10 million years (Appenzeller and Mundt, 1989). The name for the star type comes from the prototype star T Tauri in the Taurus star-forming region. The T Tauri stars are pre-main-sequence stars with masses less than $3 M_{\odot}$. The T Tauri stars are found near the molecular clouds and are identified by their optical variability and strong chromospheric lines.

TW Hya is a 10 Myr old star which shows close resemblance to our Sun with a mass of only $0.8 M_{\odot}$ (Bergin et al., 2013). TW Hya is categorized to have a spectral type of K6Ve while our sun has a spectral type of G2V (Torres et al., 2006). Alongside the very close spectral type the star also shows a close resemblance to the sun in terms of its mass. With a distance of 54 ± 6 pc TW Hya is a relatively close star (Qi et al., 2013). What makes TW Hya particularly interesting is the face-on viewing angle (inclination of $\sim 6^{\circ}$) of the star

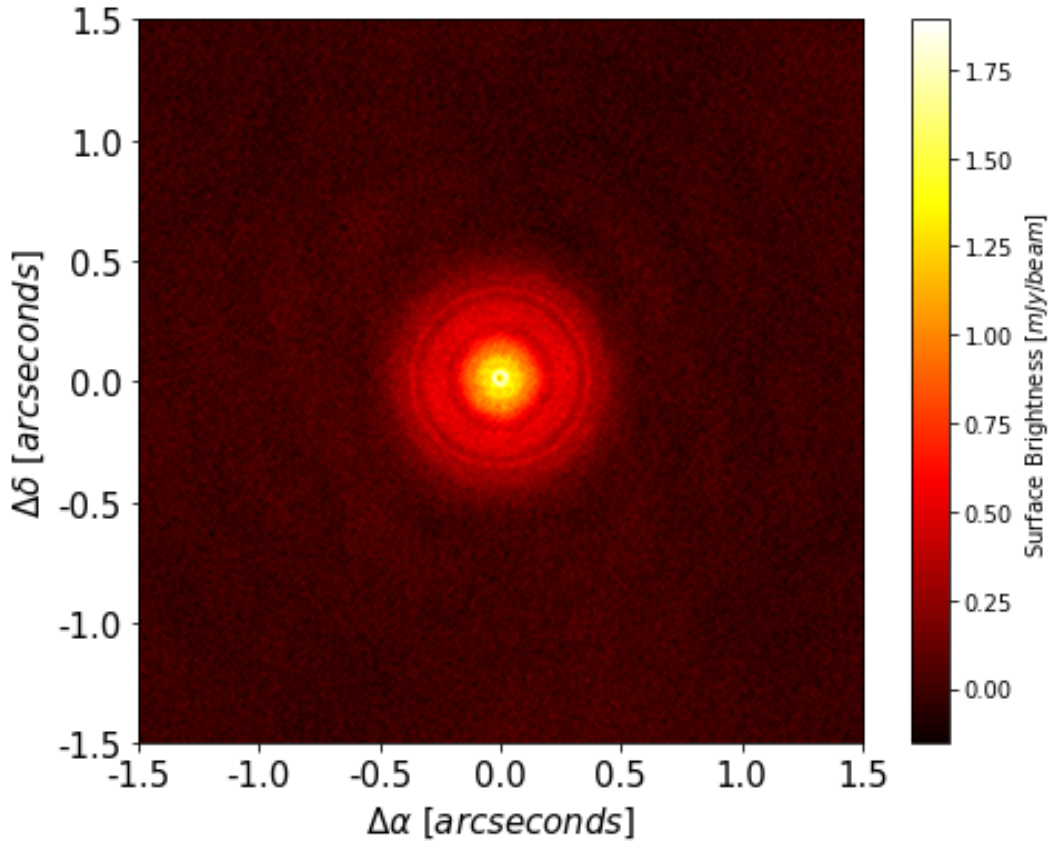


FIGURE 1.1: Image of the $870\mu\text{m}$ continuum emission of TW Hya disk with a 30 mas FWHM (1.6 AU) circular beam. The rms noise level is roughly $35\ \mu\text{Jy beam}^{-1}$ (Andrews et al., 2016).

and its gas-rich disk with a disk-mass of $\sim 0.04\ M_{\odot}$ (Bergin et al., 2013). The disk size as traced by millimeter dust emission is ~ 60 AU, with a more extended (> 100 AU) disk in gas emission (CO) and micrometer-sized dust emission (Andrews et al., 2012). Within this disk around TW Hya, Setiawan et al. (2008) have postulated a planet of mass $9.8 \pm 3.3\ M_{\text{Jup}}$ which orbits the star with a period of 3.56 days at 0.04 AU, inside the inner rim of the disk. However, there is some discussion whether or not this planet really exists. Therefore this observation should be addressed carefully. If this planet exist, it would demonstrate that planets can form within 10 Myr, before the disk has been dissipated by stellar winds and radiation. The recent image of TW Hya as observed by ALMA can be seen in Fig. 1.1. In this figure the protoplanetary disk of TW Hya shows three distinctive rings around the center. If the earlier postulated planet orbiting at 0.04 AU is causing one of these observed rings could be debated. Earlier observations have shows that one planet could cause multiple gaps, so the relation between this planet and the substructure remains to be checked (Bae, Zhu, and Hartmann (2017), Dong et al. (2017)).

1.5 Surface brightness

A deprojection of the ALMA observations of these gaps in the protoplanetary disk is shown in Fig 1.2. In this figure by Andrews et al. (2016) they show the surface brightness of the ALMA $870\ \mu\text{m}$ observations of TW Hya and its protoplanetary disk that trace millimeter-sized particles down to spatial scales as small as 1 AU (20 mas). In these images the rings are clearly visible with the contrast between the dark and bright annuli between 5% - 30%.

In Figure 1.2 we see the image as previously shown in Fig. 1.1 now azimuthally averaged into a radially surface brightness profile. The inner disk (<0.5 AU in radius) includes an unresolved source coincident with the stellar position (0.93 ± 0.04 mJy) and a bright ring that peaks at 2.4 AU. Between these two features a dark annulus is centered at a distance of 1 AU. The bright ring and dark annulus are unresolved (<1 AU across). Because of this resolution issue it is difficult to estimate the depth of the dark annulus unambiguously, but they find at least a 30% brightness reduction.

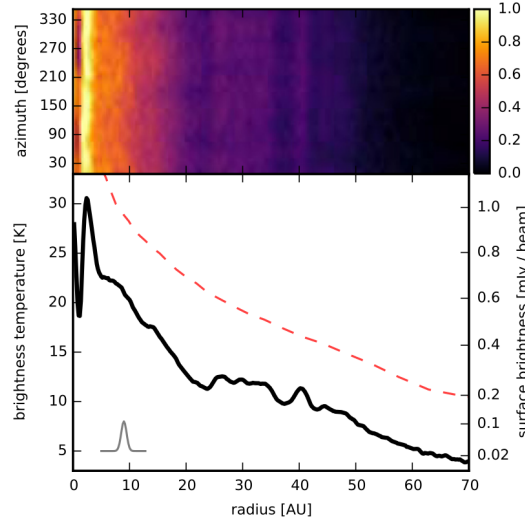


FIGURE 1.2: (top) High resolution (24×18 mas beam) synthesized image deprojected into a map in polar coordinates to more easily view the disk substructure (bottom). The azimuthally averaged radial surface brightness profile. For reference, the dashed red curve shows the midplane temperature profile derived from a representative model disk. The gray curve in the bottom left reflects the profile of the synthesized beam (figure and caption taken from Andrews et al., 2016, Fig.2)

1.6 Surface density

The SPHERE observations of TW Hya by van Boekel et al. (2017) probe the sub-micron-sized dust population in the disk surface that closely follows the bulk gas density. Their SPHERE observations have a spatial resolution of 1-2 AU, which is similar to ALMA dust continuum observations. Motivated by the strong radial variations in the surface brightness and high degree of azimuthal symmetry in their observations, they focus their analysis on explaining these radial variations. Their main interest is the bulk surface density profile of the TW Hya disk. To examine the surface density profile they have developed a radiative transfer model of the TW Hya disk. The radiative transfer model has independent distributions of coupled gas and small dust as traced by the SPHERE observations on the one hand, and large dust as traced by the ALMA observations on the other (van Boekel et al., 2017).

Their radiative transfer model has small dust grains following an MRN size distribution with grain radius $a_{\min,s} \leq a_{\max,s}$; the large dust also follows an MRN size distribution with $a_{\min,l} \leq a_{\max,l}$. They argue that radial variations in the gas density may lead to radial drift of dust particles that are large enough to no longer be perfectly coupled to the gas, yet small enough to still be influenced by it (i.e., particles with Stokes numbers not largely different from unity). Their surface density of large grains, ranging from 1-10 mm, is shown

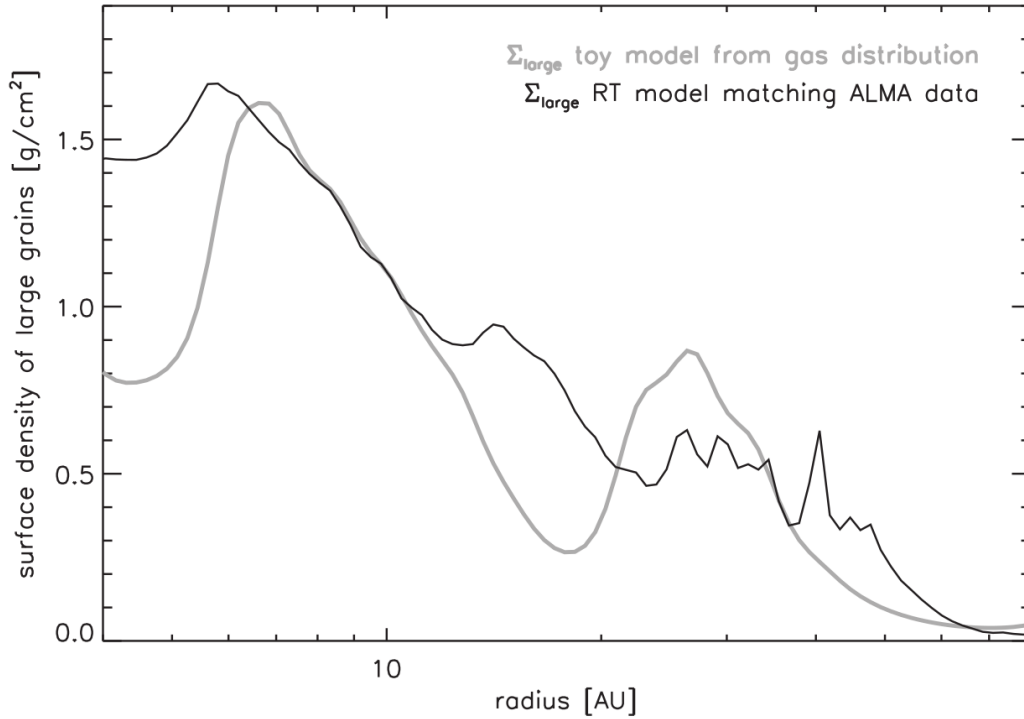


FIGURE 1.3: Figure 18 from van Boekel et al. (2017): Toy model for the radial distribution of large dust derived from the gas distribution in their radial transfer model (grey) compared to the radial distribution of large grains that reproduces the ALMA data (black). A distance of 54 pc has been assumed.

in Fig. 1.3. In this figure, the black line represents the surface brightness, obtained from their radiative transfer model, matching the ALMA data by Andrews et al. (2016). In this figure the grey line represents the large dust grain surface density as it would arise from their SPHERE gas model taking into account how the large grains are drifting in such a "gas disk". The black line shows the radial distribution of large grains that they find from directly fitting the ALMA data. van Boekel et al. (2017) note that the absolute level of the surface density of large grains in the ALMA data is not well determined. With their assumed large grain sizes of 1–10 mm they obtained an opacity of $\sim 1 \text{ cm}^2 \text{ g}^{-1}$ for the large grains.

They also explore the possibility where embedded planets are responsible for creating the gaps and estimate the corresponding limits of planet masses following Debes et al. (2013). Duffell (2015) has created a simple analytical model to model the gaps in the protoplanetary disks. He presents a model for calculating the surface density as a function of radius in which a planet has opened a gap. The comparison between their derived depletion factor ($f(R)$) and an implication of the model of Duffell (2015) is shown in Fig. 1.4. They conclude that the TW Hya disk gaps are only partially cleared, which implies that, if planet-disk interaction is the underlying physical mechanism, the embedded planets have masses that are substantially below the gap opening mass. This gap opening mass is dependent on the viscosity parameter α ; if α increases then the mass required to reach a given gap depth is higher.

Alongside the surface density of the large grains the surface density of the gas is also investigated. The gas surface density from their model matching the SPHERE data is shown in Fig. 1.5.

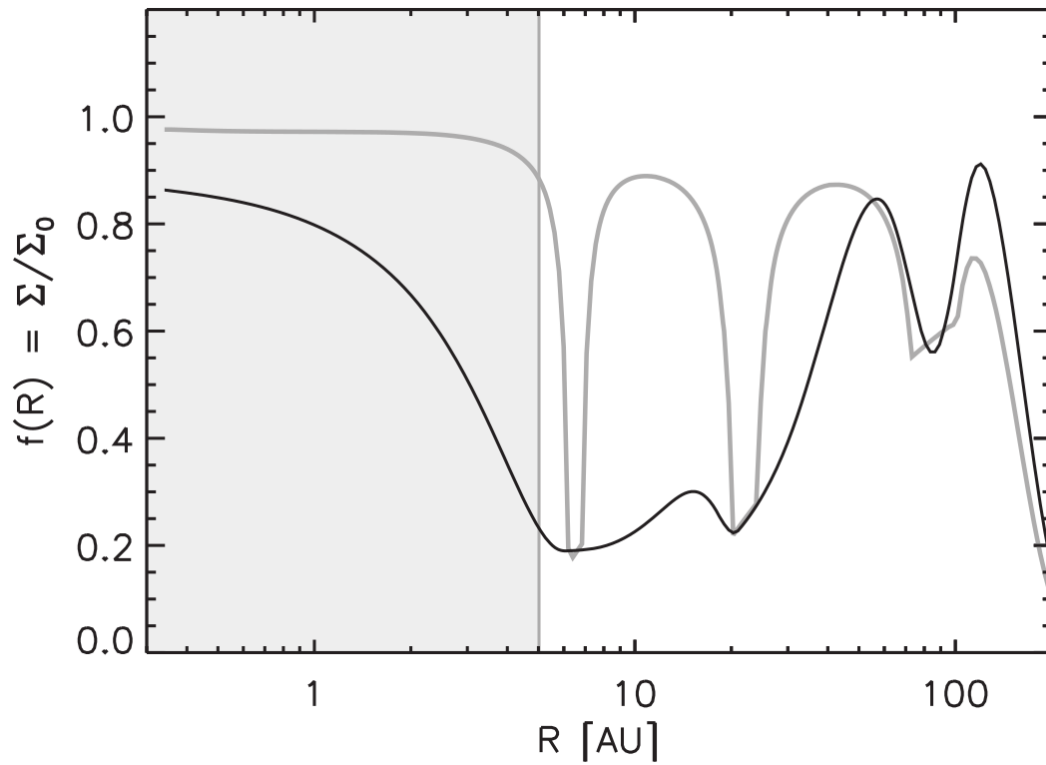


FIGURE 1.4: Comparison between the derived radial surface density depletion factor ($f(R)$, black curve) and an implementation of the model of Duffell (2015) with three planets, approximately matching the depth of the gaps (gray curve). The innermost disk regions that are not well probed with the observations are masked. A distance of 54 pc has been assumed (figure and caption from van Boekel et al., 2017).

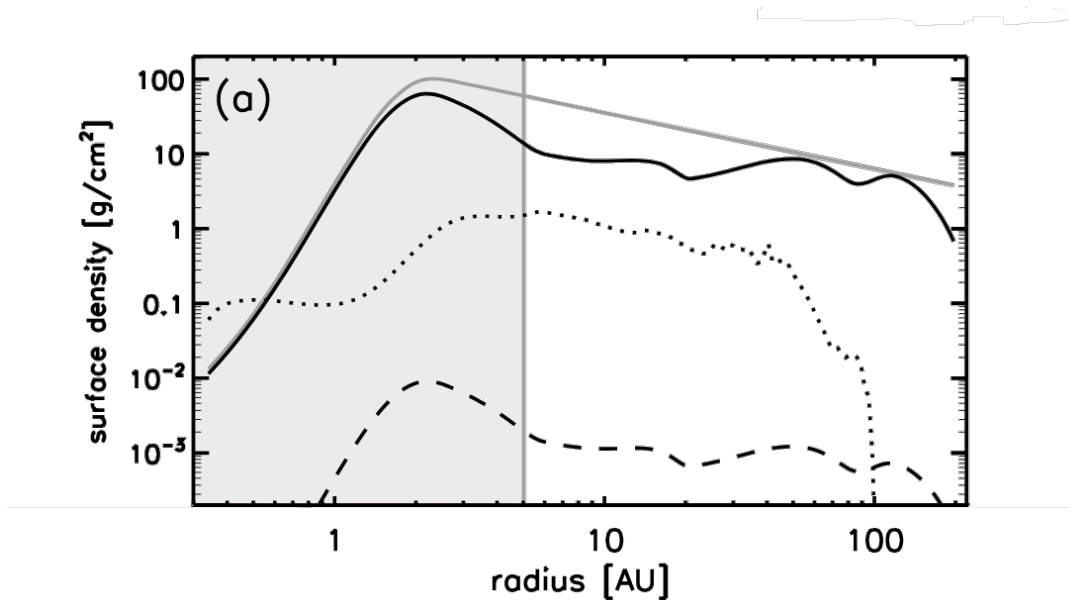


FIGURE 1.5: Figure 11.a from van Boekel et al. (2017), the black line denotes the gas surface density from their model. The grey line represents the unperturbed surface density profile from Menu et al. (2014). The surface density of small grains is indicated with the dashed line, and the population of large grains near the midplane is shown with the dotted line.

1.7 Chemistry

CO is the second most abundant species in molecular clouds reaching values of 10^{-4} of the H_2 abundance (Maciel, 2013). The collision between the H_2 molecules and the CO molecules produce CO rotational level excitation, followed by emission of photons at mm wavelengths. The CO chemical bond is extremely strong with r_0 being unusually small. The reason to choose CO over H_2 is that H_2 has no dipole moment and the H_2 rotational lines have excitation energies much larger than 100 K. The rotational levels of CO are much more closely spaced than those of H_2 , meaning there are many more allowed rotational levels (Draine, 2011).

The CO rotational lines span a wavelength range from infrared to a few mm. The CO 2.6 mm line in a galaxies molecular gas plays the same role as the atomic H 21 cm line in the mapping of diffuse interstellar gas (Maciel, 2013). Alongside the CO emission lines the CO iceline is also investigated. This line shows the temperature at which the CO molecules freeze out onto cold dust grain surfaces.

1.8 Aim

The aim of the project is to adapt the surface brightness of an existing disk model of TW Hya in such a way that it would match the new higher spatial resolution ALMA observations. This existing disk model and the thermo-chemical disk code called ProDiMo will be introduced in Chapter 2. ProDiMo calculates both, the continuum radiative transfer and the gas thermal balance/chemistry. This original model will be adapted in order to investigate to which extent the inhomogeneous dust distribution causes similar structures in the gas - either thermal or chemical inhomogeneities - and whether these would be observable with ALMA in the CO submm gas lines. Chapter 3 explains in detail how the original model will be adapted to show the substructure as observed by Andrews et al. (2016) (Fig. 1.2). In chapter 4 the results will be presented and the influence of this substructure on the gas will be discussed. In chapter 6 and 5 I will give a short summary after which we will draw our conclusions and discuss the obtained results.

Chapter 2

The model

The protoplanetary disk of TW Hya and the host star will be modeled using the thermo-chemical disk code ProDiMo that calculates both, the continuum radiative transfer and the gas thermal balance/chemistry. ProDiMo is an acronym for Protoplanetary Disk Model. ProDiMo assumes a steady state solution for the calculation of the disk properties. It is based on the thermo-chemical models of Kamp and Bertoldi (2000); Kamp and van Zadelhoff (2001); Kamp and Dullemond (2004), but completely re-written to be more flexible and to include more physical processes (Woitke, Kamp, and Thi, 2009).

ProDiMo calculates the physical, thermal and chemical structure of a protoplanetary disk using global iterations. These iterations involve 2D dust continuum radiative transfer, gas-phase and photo-chemistry, thermal energy balance of the gas, and the calculation of the hydrostatic disk structure in axial symmetry. Alongside these physical parameters ProDiMo also calculates some observables such as images and lines.

One of the main advantages of using ProDiMo is the flexibility in the code. Different aspects of the model can be ignored or skipped based on the specific problem. These so-called "switches" make sure that small adaptations of a model can be implemented within limited computational time. In this thesis the aim is to fit an existing model to recent observations by an iterative procedure of minimizing the difference between observations and model. These switches make it easy to speed up the runtime for each model. It is also possible to restart a run with adaptations from a checkpoint file created after every run, which is frequently used in this thesis. Alongside restarting from this checkpoint file, the chemistry will also be kept constant for the different adaptations.

After every run ProDiMo creates a restart file which could be used as a checkpoint file to improve the speed of the reruns as a number of calculations are skipped and just taken from the checkpoint file. In this way, the model starts the adaptations from a known "good" solution. In this thesis adaptations of a standard model will be run over each other in order to match the model surface brightness profile to an image surface brightness profile as good as possible. As there is no need to calculate the chemistry and temperature of the in between runs, but only for the final run, the chemistry switch is turned off. After a satisfactory match is obtained between the image profile and the model profile, the chemistry will be calculated for that specific run to compare to the initial DIANA model.

2.1 Data visualization with ProDiMopy

The output from ProDiMo can be visualized with the help of ProDiMopy. ProDiMopy is a python package which provides routines for reading and plotting the output of one or more ProDiMo models. The output of the models can also be processed using an idl script,

however this method visualizes all the output from the model in a single postscript file. ProDiMopy also makes it easier to extract a specific value or values from the model which could be used for further analysis.

2.2 The DIANA project

In this thesis the aim is to adapt an existing model of the protoplanetary disk surrounding TW Hya to capture the substructure in the rings. These adaptations will start from a known model of the DIANA project. The DIANA project (The European FP7 project DiscAnalysis) aims to model a statistically relevant sample of protoplanetary disks in approximately the same way in order to compare the physical output of these models (Woitke et al., 2018a). The DIANA project has modeled a total of 27 protoplanetary disks and their host star using the same methodology in order to compare the derived physical disk properties from these models. Currently, the assumptions for disk modeling vary significantly between papers, making it rather difficult to compare these properties, even if they originate from the same research group. Contrary to many earlier efforts, in the DIANA project these physical and chemical modeling assumptions are not changed as they are applied to different objects.

The approach of the project is based on a defined succession of three modelling steps. First, the aim is to fit the stellar and irradiation properties of the central stars. Second, applying state-of-the-art 2D disk modeling software ProDiMo, which will also be used in this thesis, with a fixed set of physical and chemical assumptions, to simultaneously fit the disk shape, dust opacity and gas parameters of all objects. Finally, to use various post-processing radiative transfer tools, including FLiTs (written by M. Min) (Woitke et al., 2018a).

The TW Hya image used by the DIANA project is 854 μm ALMA archival data. This data set has a resolution of 1.5" which is lower compared to the 30 mas FWHM circular beam image which will be used for this thesis. The comparison of this original low resolution input profile and the surface brightness profile of the DIANA model is shown in Fig. 2.1.

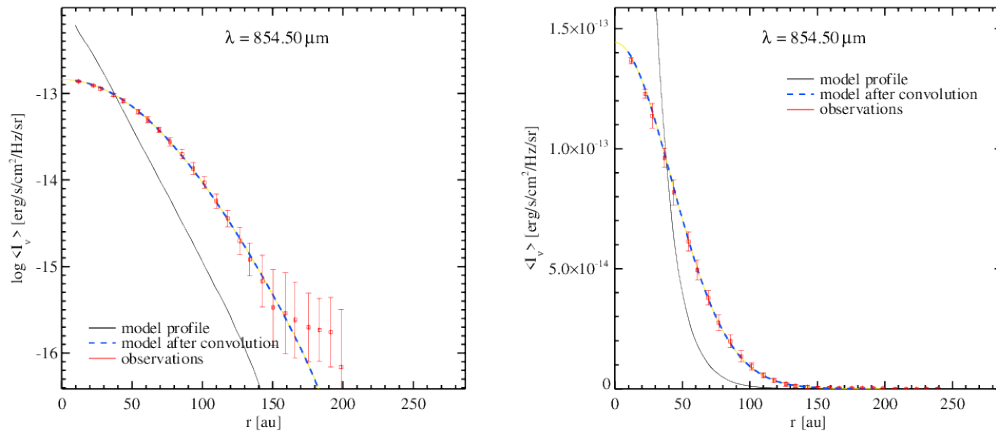


FIGURE 2.1: The surface brightness profiles from the DIANA model at 854 μm . Left shows a logarithmic scale, right shows the linear scale.

2.3 Initial model parameters

The initial parameters for the model and the adaptations which will be done during this thesis are taken from the DIANA model. The region where the hydrogen nuclei particle density reaches 10^{20}cm^{-2} is defined as the outer edge of the disk. The initial conditions set for TW Hya and its protoplanetary disk are shown in Table 2.1.

Stellar parameters	
Stellar mass	0.75 M_{\odot}
Stellar luminosity	0.242 L_{\odot}
Stellar effective temperature	4000.0 K
Disk parameters	
Inner disk	0.078 -4.6 AU
Gas to dust ratio inner disk	781
Outer disk	4.6-180 AU
Gas to disk ratio outer disk	441
Disk mass	$4.48 \times 10^{-2} M_{\odot}$
Distance	51 pc
Inclination	7 degrees
Dust parameters	
Minimum grain radius	$1.14 \times 10^{-3} \mu\text{m}$
Maximum grain radius	$5.73 \times 10^3 \mu\text{m}$
Dust size distribution power index	4
Chemistry	
Number of species	239
Number of elements	14

TABLE 2.1: Input parameters for ProDiMo taken from the original DIANA model for TW Hya (Woitke et al., 2018a).

Chapter 3

Method

The aim of the project is to investigate how the substructure of the disk influences the gas either in a thermal or chemical way. The DIANA model, as described in Sect. 2.2, will be the starting point. This DIANA model will be modified to match to an observed brightness profile as good as possible.

3.1 Surface brightness

While digitizing the surface brightness from Andrews et al. (2016) (Fig. 1.2) it could be noticed that the intervals between the axis label on the right vertical axis are not linear between 0 – 0.2 mJy/beam. As the distance on this axis is the same between 0.02 – 0.2 mJy/beam as it is between 0.2 – 0.4 mJy/beam, the determination of the profile from this paper ended in values below zero after ~ 60 AU. In the higher frequency ALMA bands which were used for the determination of this profile the Rayleigh-Jeans criterion is not

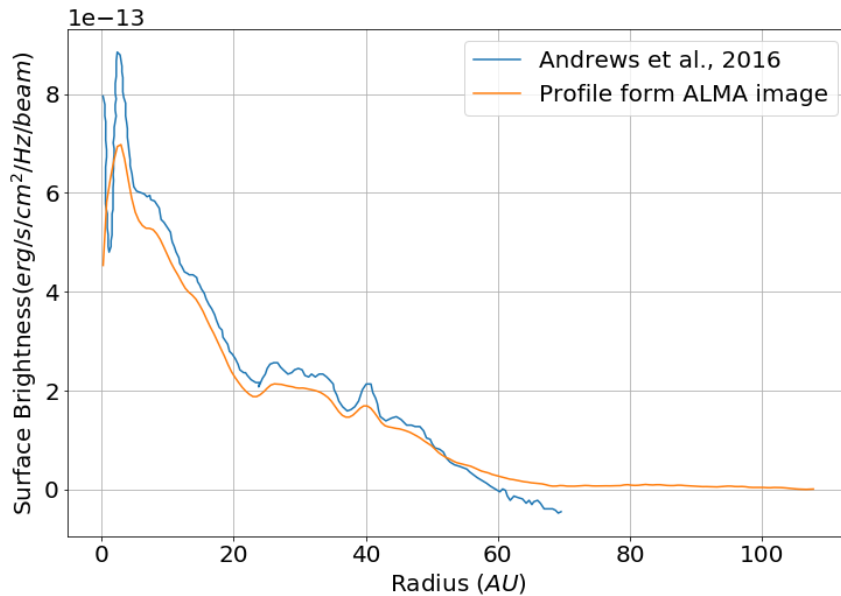


FIGURE 3.1: The original surface brightness profile as determined by Andrews et al. (2016) (blue) versus the newly determined surface brightness profile from their image shown in Fig. 1.1 (yellow). Their original profile drops to negative values for the surface brightness after ~ 60 AU, while the newly determined surface brightness profile goes asymptotically to zero. In this thesis, the surface brightness profile as determined from the ALMA image will be used from here on as the Andrews et al. (2016) surface brightness.

met. Therefore, the brightness temperature is calculated from the full plank function, as this is a more appropriate way to compare the brightness temperature with the surface brightness. The surface brightness profile is determined from the ALMA image showed in Fig. 1.1¹, using the 30 mas circular beam instead of the 24×18 mas beam as described in Fig 1.2. This new surface brightness profile is determined by Christian Rab from the original image as referred to in the Andrews et al. (2016) paper. The comparison between these two profiles is shown in Fig. 3.1. Here the original profile from Andrews et al. (2016) is shown in blue, and the new determined profile is shown in yellow. From this figure it can be seen that the profile as determined by Andrews et al. (2016) is indeed taking negative values after 60 AU, while the new profile is asymptotically going to zero. In this thesis, the ALMA image determined surface brightness profile will be used as the Andrews et al. (2016) surface brightness.

3.1.1 Determining the model surface brightness

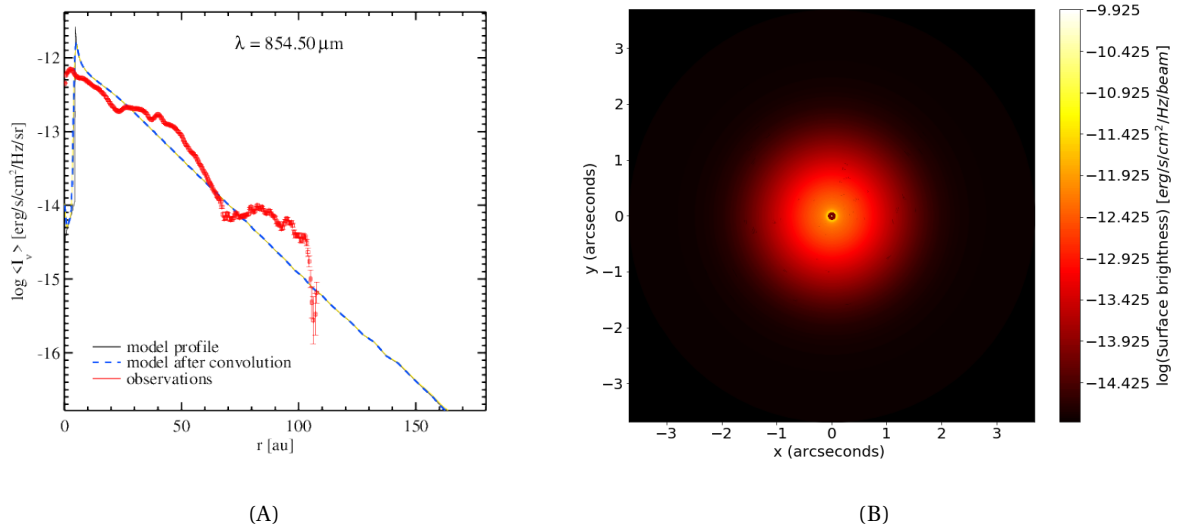


FIGURE 3.2: Figure 3.2A shows the image profile by Andrews et al. (2016) (red) in comparison to the model surface brightness profile before (black) and after convolution with the ALMA beam (blue dashed). Figure 3.2B shows the image representation of the DIANA model surface brightness profile.

ProDiMo uses two types of grids; one for the physical disk structure and one for the ray tracing to obtain images. For the determination of the surface brightness the latter is used. The data in the ray tracing grid is polar and is determined at 300 different wavelengths. The profile by Andrews et al. (2016) is from the $870 \mu\text{m}$ continuum image, the closest matching wavelength will be used for the comparison, which corresponds to $865 \mu\text{m}$. The model calculates the image by creating rings at increasing radii originating from the center of the star. Each of these rings then consists of 72 data points at which the values for the brightness are calculated in $\text{erg/s/cm}^2/\text{Hz/sr}$. The annuli are separated logarithmically in radius. The radial profile is calculated by taking the mean over each of the separate rings, resulting in a value for the surface brightness corresponding to the radius of that ring.

¹Image taken from <https://www.cfa.harvard.edu/sandrews/data/twhya/>

The radial surface brightness profile as determined by Andrews et al. (2016) has units of mJy/beam. In order to convert from per beam to per steradian the values as determined by Andrews et al. (2016) are multiplied by 3283.8 (1 sr = 3283.8 degrees²) and divided by the area of the beam in degrees². The area of the beam is defined as

$$\Omega = \frac{\pi b_{\text{maj}} b_{\text{min}}}{4 \ln(2)} \quad (3.1)$$

This equation assumes a beam with $b_{\text{min}} = 30$ mas and $b_{\text{maj}} = 30$ mas. This gives a total area of 7.87×10^{-11} degrees². The comparison of the standard model of the DIANA project versus the image data as determined by Andrews et al. (2016) is presented in Fig. 3.2. In this figure the blue line represent the radial surface brightness from the DIANA model, the red line represents the ALMA data by Andrews et al. (2016). Figure 3.2 shows that the DIANA model and the ALMA image data are in the same order of magnitude and have roughly the same shape. However, from 70 -100 AU the DIANA model is underestimating the surface brightness by a factor ~ 5 .

3.1.2 Adapting the model

The current DIANA model will be adapted to match the observations done by Andrews et al. (2016). For each radial point the value for the surface brightness of the original DIANA model is divided by the value of the image data as determined by Andrews et al. (2016), resulting in a factor $f_{I/M}$. The column density for the DIANA model will be multiplied by $f_{I/M}$, creating a new column density which will be used for the next run. The column density used for the DIANA model is shown in Fig. 3.4 in blue. As the main interest of this thesis is the outer region of the disk, the inner region of the column density will be kept constant. This corresponds to just before the big jump at 4.5 AU, where the column density increases by a factor of ~ 4000 .

The profile beyond 4.5 AU will be multiplied by $f_{I/M}$. Since the factor will increase or decrease based on the difference between the model and the image, this behaviour translates to an increasing and decreasing column density corresponding to the observed rings. This process is repeated several times until the model and the image data are of roughly the same shape. This procedure has previously established by Muro-Arena et al. (2018) for HD163296. They have modeled the disk was using the Monte Carlo radiative transfer code MCMax3D where they have modeled the radial dust surface density profile after the ALMA observations.

3.1.3 Calculating $f_{I/M}$

ProDiMo calculates the images of the protoplanetary disk using a polar grid with 275 radial and 72 azimuthal data points. These radial data points extend out to a distance of ~ 200 AU, while the observed image profile by Andrews et al. (2016) extends out to ~ 125 AU. The image profile observes only the dust, while the aim is to model the gas as well. Therefore the image profile is extrapolated out to 200 AU in order to calculate the factor, $f_{I/M}$. This extrapolation resulted in a new image profile out to 200 AU. However, as the original image profile by Andrews et al. (2016) has values close to zero around 125 AU, the extrapolation of this profile resulted in the extended profile having the value of zero from 130 AU to 200 AU. If $f_{I/M}$ were to be calculated using these two profiles, $f_{I/M}$ drops to zero for radii

> 125 AU. For the follow-up procedure of multiplying the column density with $f_{I/M}$ this results in a zero-value column density from 125 AU to 200 AU.

The better approach to calculating $f_{I/M}$ is to create a new image profile for the surface brightness by combining the original image profile as determined by Andrews et al. (2016) and the surface brightness from the DIANA model. Up to ~ 80 AU this new profile will be exactly the same as the image profile by Andrews et al. (2016). After ~ 110 AU this profile will be exactly the same as the DIANA model profile. In between these boundaries a weighted average of the image surface brightness and the model surface brightness is calculated. This new image surface brightness profile is then divided by the model surface brightness profile to create a new factor called $f_{W/M}$. This factor is shown in Fig. 3.3 in red. What can be seen here is that this new $f_{W/M}$ is lower by a factor 2 with respect to $f_{I/M}$. For the calculation of $f_{W/M}$ for the first run the weighted average is calculated between 78.07 AU and 105.88 AU. ProDiMo creates a new image grid every time it is rerun, causing the intervals in which the weighting occurs to vary from one run to the other. However, this variation is at most 1 AU.

As none of the two previous factors show the desired behaviour, they are combined. Up to ~ 110 AU the factor $f_{I/M}^{final}$ is equal to the factor calculated from extrapolating the image profile, thus capturing all the structure. After ~ 110 AU $f_{I/M}^{final}$ is equal to $f_{W/M}$. This means that the two previously calculated factors are glued together at 110 AU to create the final $f_{I/M}$, $f_{I/M}^{final}$ which will be used from here on. This $f_{I/M}^{final}$ is shown in Fig. 3.3 as the black line.

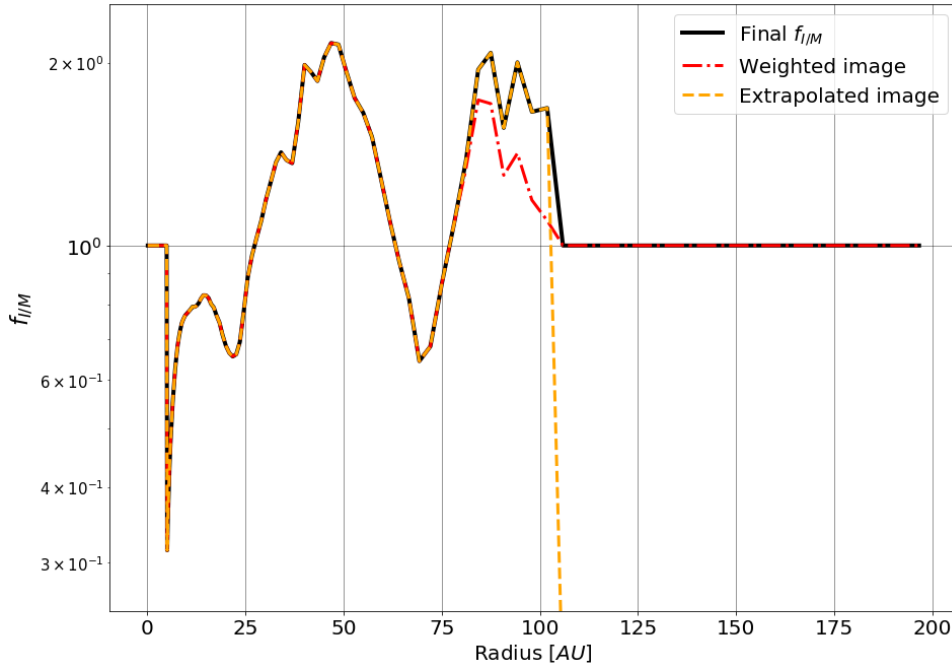


FIGURE 3.3: Three different $f_{I/M}$ which are determined. The original $f_{I/M}$ which drops to zero (green), $f_{W/M}$ as calculated between the weighted image profile and the model profile (red), and the factor $f_{I/M}^{final}$ which is eventually used for the determination of the new column density (black). As the inner disk is ignored, the $f_{I/M}$ is fixed to be 1 between 0–4.5 AU. Note that the three different $f_{I/M}$ are the same up to 75 AU.

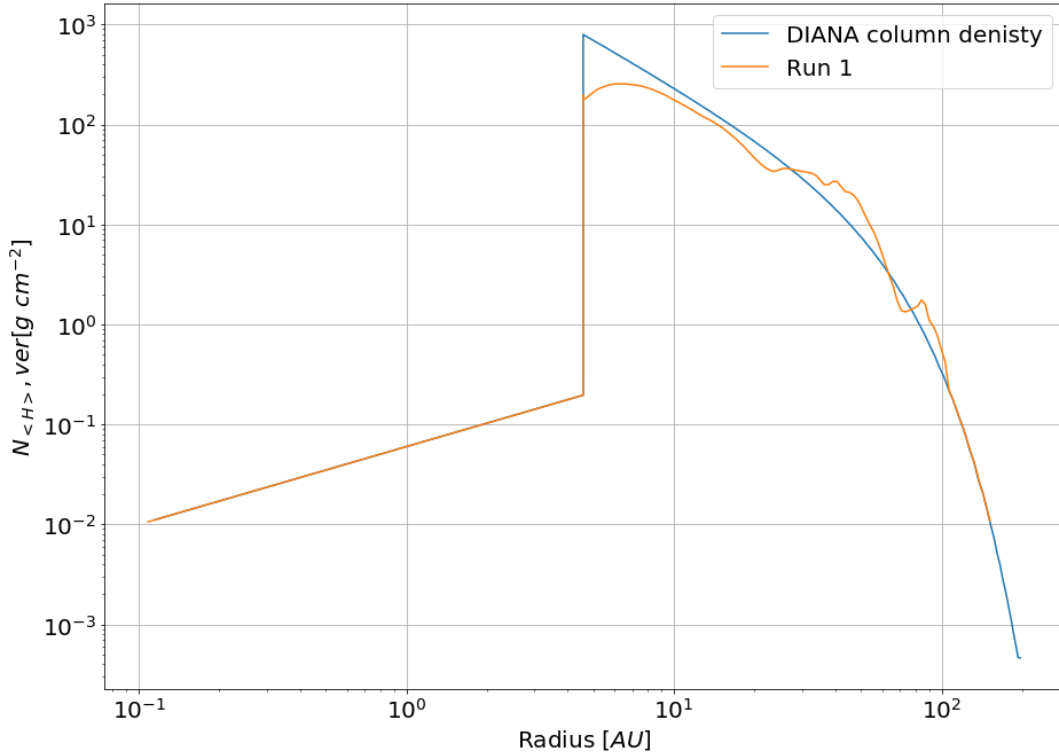


FIGURE 3.4: The comparison of the number densities before and after the procedure described in this section. In blue the original smooth number density used in the DIANA standard model, in yellow the first adaptation of the profile already showing some of the substructure. The inner disk, up to 4.5 AU, is kept the same as the initial model.

3.1.4 Manipulating the column density

The original column density is multiplied by $f_{I/M}^{final}$. From this the new column density is created which will be used for the first run. This new column density is shown in Fig. 3.4. As previously discussed, the inner disk will be kept constant with respect to the original DIANA run which can be seen in Fig. 3.4. Here it can be seen that the two profiles are overlapping and the first adaptation of the profile is occurring after 4.5 AU. In the region between 4.5 – 27 AU the surface density is decreasing, which is as expected since the DIANA model overestimated the surface brightness in this region. The column density is increased between 27 – 62 AU, corresponding to the underestimation of the DIANA model in this region. Between 62 and 75 AU the profile shows a small dip, which can also be seen in Fig. 3.2A. In the region between 75 – 106 AU the profile increases again, after which it follows the previous column density exactly.

3.2 Surface density

The final surface density will eventually be compared to the final surface density profile from the van Boekel et al. (2017) model. This profile is shown in Fig. 1.5. In this profile they show the gas surface density of the TW Hya disk. This surface density can be calculated from the vertical hydrogen column density by multiplying by the mean molecular weight of the gas and the mass of hydrogen. Here a mean molecular weight of $\mu = 2.4$ is assumed.

The surface density of large grains of the final model is also compared to the van Boekel et al. (2017) model profile for large grains. Their profile showing the surface density of large grains is shown in Fig. 1.3. In this model they have created a radiative transfer disk model with self consistent temperature and vertical structure iteration and including grain size-dependent dust settling. They have fitted the SPHERE and ALMA data, with their SPHERE observations having a resolution of 1-2 AU, similar to recent ALMA dust continuum observations.

Figure 1.3 only shows the surface density of the large grains (sizes between 1 – 10 mm), while the models for this thesis calculate the surface density for the gas disk. To correct for this the model profile will be divided by the gas to dust ratio as given in the DIANA model. This gas to dust ratio has a value of 781 in the inner disk (< 4.5 AU) and 441 in the outer regions. In this thesis the focus is on the outer region, therefore the profile will be divided by 441 to account for the dust instead of the gas.

Once the surface density of the grains is calculated, the profile needs to be corrected for the different grain size distributions. van Boekel et al. (2017) have used two intervals in which the surface density is calculated. First, the interval between $0.1\mu\text{m}$ to $3\mu\text{m}$ for the small grains, and 1 - 10 mm for the large grains. Both of these intervals follow an MRN size distribution. The DIANA model, which will be used as the starting model, here used a continuous grain size distribution between $a_{\min} = 1.141 \times 10^{-3} \mu\text{m}$ and $a_{\max} = 5.735 \times 10^3 \mu\text{m}$. In order to correctly compare the two profiles, the surface density in large mm grains will be extracted from the DIANA model to match the interval of the large grains only. The fraction between the total mass and the mass of the large grain particles will be calculated as follows. The total mass of grains between sizes a_{\min} and a_{\max} is defined as

$$M_{\text{dust}} = \int_{a_{\min}}^{a_{\max}} n(a) \cdot m(a) da \quad (3.2)$$

where the mass of a single particle is defined as

$$m(a) = \frac{4}{3} \pi \rho_{\text{grain}} a^3 \quad (3.3)$$

and the grain size distribution is defined as

$$n(a) \sim a^{-\gamma} \quad (3.4)$$

In the interstellar medium, the power for the grain size distribution (γ) is equal to 3.5, while the DIANA model has $\gamma = 4$. Together with the maximum and minimum radii from this DIANA model, $a_{\min} = 1.141 \times 10^{-3} \mu\text{m}$ and $a_{\max} = 5.735 \times 10^3 \mu\text{m}$, the factor between the two intervals becomes

$$f_{\text{tot}/\text{large}} = \frac{M_{\text{dust,tot}}}{M_{\text{dust,1mm}-a_{\max}}} = \frac{\int_{a_{\min}}^{a_{\max}} a^{-4} \frac{4}{3} \pi \rho_{\text{grain}} a^3 da}{\int_{1 \text{ mm}}^{a_{\max}} a^{-4} \frac{4}{3} \pi \rho_{\text{grain}} a^3 da} \quad (3.5)$$

Important to note here is that van Boekel et al. (2017) have a maximum grain size of 10 mm while the maximum grain radius in the DIANA model is $a_{\max} = 5.735 \text{ mm}$. Therefore the integration boundaries of the interval of the large grains are between 1 mm and a_{\max} , and not between 1 mm and 10 mm. With this in mind the integral becomes

$$f_{\text{tot/large}} = \frac{\int_{a_{\text{min}}}^{a_{\text{max}}} a^{-1} da}{\int_{1 \text{ mm}}^{a_{\text{max}}} a^{-1} da} = \frac{\ln a_{\text{max}} - \ln a_{\text{min}}}{\ln a_{\text{max}} - \ln 1 \text{ mm}} = 8.83 \quad (3.6)$$

The output from the model by van Boekel et al. (2017) will be compared to the surface density as calculated by the final run of adaptations to the original DIANA model.

3.3 Chemistry

To investigate how this substructure of the disk is influencing the chemistry in the protoplanetary disk of TW Hya the gas and dust temperature as well as the CO abundance distribution from the original DIANA model will be compared to the final iteration of the run with the adapted column densities.

At first it will be investigated how the dust temperature is changing with radius and depth of the disk. Second, the gas temperature is investigated in the disk. Third, the CO iceline showing where the CO molecules occur as ice is compared. Finally, the fluxes of three isotopologues of the CO molecule; ^{12}CO , ^{13}CO and C^{18}O will be compared.

Chapter 4

Results

4.1 Surface brightness

4.1.1 First run

The adaptations of the model to match the surface brightness profile as determined by Andrews et al. (2016) are started from the DIANA model. To speed up the computational time of each rerun, ProDiMo will take the temperature from the restart file from the DIANA model such that the radiative transfer starts from a "good" solution already. In addition, neither the gas temperature nor the chemistry is calculated for the intermediate iterations.

Figure 4.1 shows the output after the first run with the new column density as shown in Fig. 3.4. Figure 4.1A shows the surface brightness of the model after convolution (blue), versus the observed surface brightness by Andrews et al. (2016) (red) on a logarithmic y-axis. In comparison to the original DIANA model, which was the starting point, it can be seen

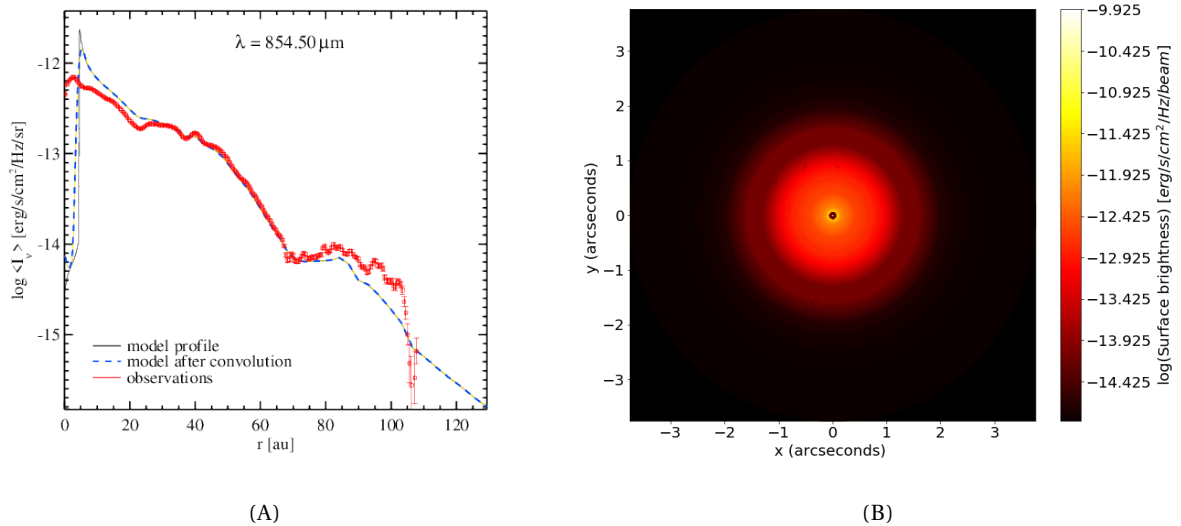


FIGURE 4.1: Output for the first run with adaptations. Figure 4.1A shows the image data by Andrews et al. (2016) (red) in comparison to the model surface brightness profile before (black) and after convolution with the ALMA beam (blue dashed). Figure 4.1B shows the image representation of this surface brightness profile.

that up to ~ 30 AU the model is still overestimating the surface brightness. However, this method has been very successful for the region $30 \leq r \leq 70$ AU, where the model and the observations are now approximately the same. In the outer region of the disk ($r \geq 70$ AU) the model is responding to the adapted column density as the model profile has increased in this region and is already showing a bump around 85 AU corresponding to the bump in the image profile. However, the image profile is still a factor two higher than the model profile in this region.

Figure 4.1B shows the image representation of the surface brightness profile of the model shown in Fig. 4.1A. In comparison to the original image form the DIANA model (Fig. 3.2B) it can be seen that the outer region ($> 1''$) is appearing fainter than it is in the original model. However, within the first arcsecond the disk seems almost as bright as it is for the original model. At the distance of TW Hya (51 pc), $1'' \approx 60$ AU. In comparison to the surface brightness profile as seen in Fig. 4.1A the model was not responding to the adaptations yet, thus explaining the bright inner disk.

Figure 4.1 shows that the manipulation of the column density is indeed affecting the surface brightness of the model. In order to also make the inner region (< 30 AU) and the outer region (> 70 AU) of the disk adapt to the observations, the same procedure as described in Sect. 3 will be applied again. The results of this are shown in Fig. 4.2. Figure 4.2A shows $f_{I/M}$ as calculated in this first run versus the $f_{I/M}$ as calculated between the original DIANA model and the image data. Figure 4.2B shows the new column density after applying $f_{I/M}$ to the column density used for the first run. ProDiMo assumes the disk to be spherically symmetric, therefore the column density is only calculated for half of the disk. However, the input column density for the model should be the column density for the entire disk. Therefore, to continue this procedure, the model calculated column density is multiplied by 2 to calculate the column density of the entire disk.

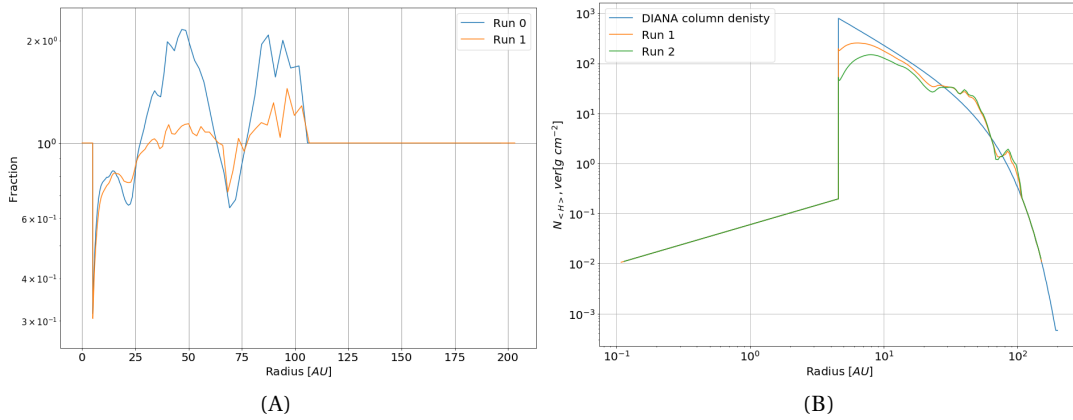


FIGURE 4.2: Figure 4.2A shows $f_{I/M}$ as calculated between the original DIANA model and the image data (blue) and $f_{I/M}$ as calculated between the first run with adaptations and the image data (yellow). Figure 4.2B shows the new column density which will be used for the second run (green) in comparison to the column density for the first run (yellow) and the original DIANA column density (blue).

4.1.2 High resolution

After three runs it became clear that the overall shape of the model surface brightness profile was matching the shape of the image surface brightness profile, but was lacking

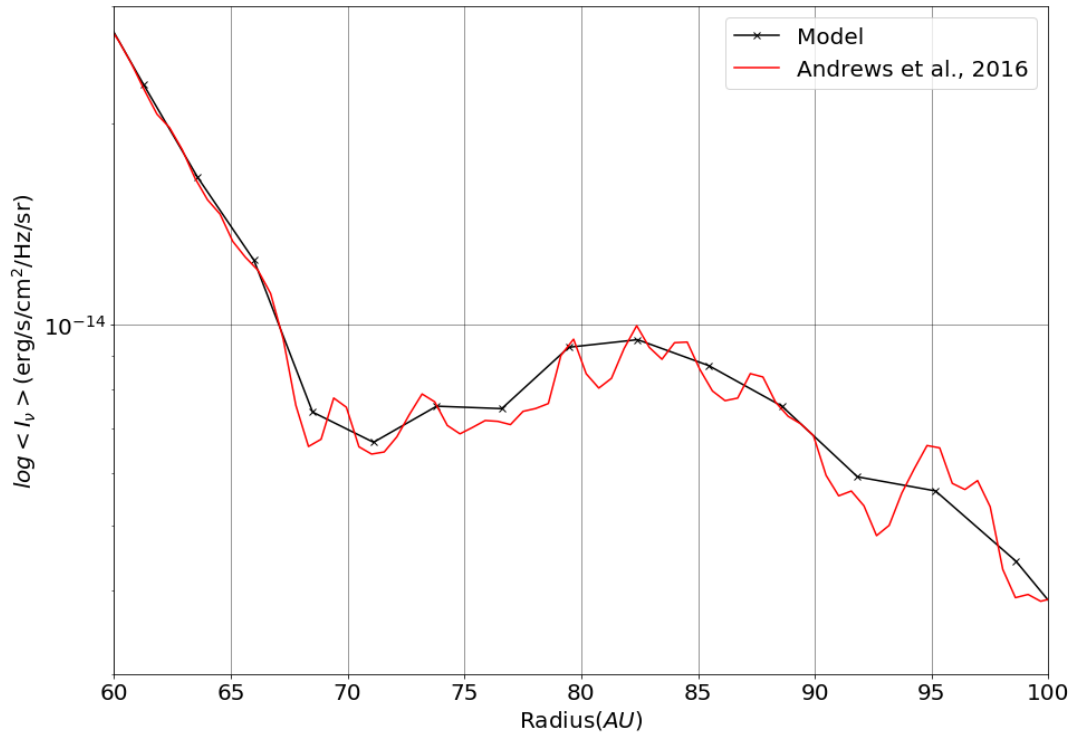


FIGURE 4.3: Model surface brightness profile (black) versus the image surface brightness profile (red) between 60 and 100 AU. This plots shows how some of the finer substructures in the image profile are not captured in the model profile as the model does not have a high enough resolution.

the finer substructures. To demonstrate this, Fig. 4.3 shows the model profile versus the image profile between 60 and 100 AU. In the model profile, the x marks a data point. What can be seen from this figure is that the finer structures of the image profile fall in between the data points. For example, the model profile matches the image profile at 79 and 83 AU. However, in between these points the image profile shows a dip. As this dip occurs in between these two points, the model profile will never catch this dip. In order to make the model profile more detailed the resolution of the model is increased. Previously the images of which the surface brightness is determined were calculated on a polar grid with 275 radial and 72 azimuthal data points. Now, the image will be calculated on a polar grid with 475 radial and 72 azimuthal data points, almost doubling the amount of points in the profile. This doubling of the data points resulted in also doubling the computation time for each run. As the amount of data point is doubled, the memory needed to run the model was also increased. Because of this the model crashed as it ran out of memory. Eventually this could be fixed by forcing the model to use less memory, increasing the computational time even further. In the end more substructure could be captured with this higher resolution, but is is not sufficient. Within the scope of this thesis exploring higher resolution models was not realistic, but it would be interesting to explore even higher resolution models in the future.

4.1.3 Background

After inspection of the fifth run $f_{I/M}$ was almost equal to one, while there was a significant difference in the surface brightness of the model versus the observed surface brightness. From here on, there are two different surface brightness figures for each run, one from an IDL script which visualizes all the output from a ProDiMo model and a python version of

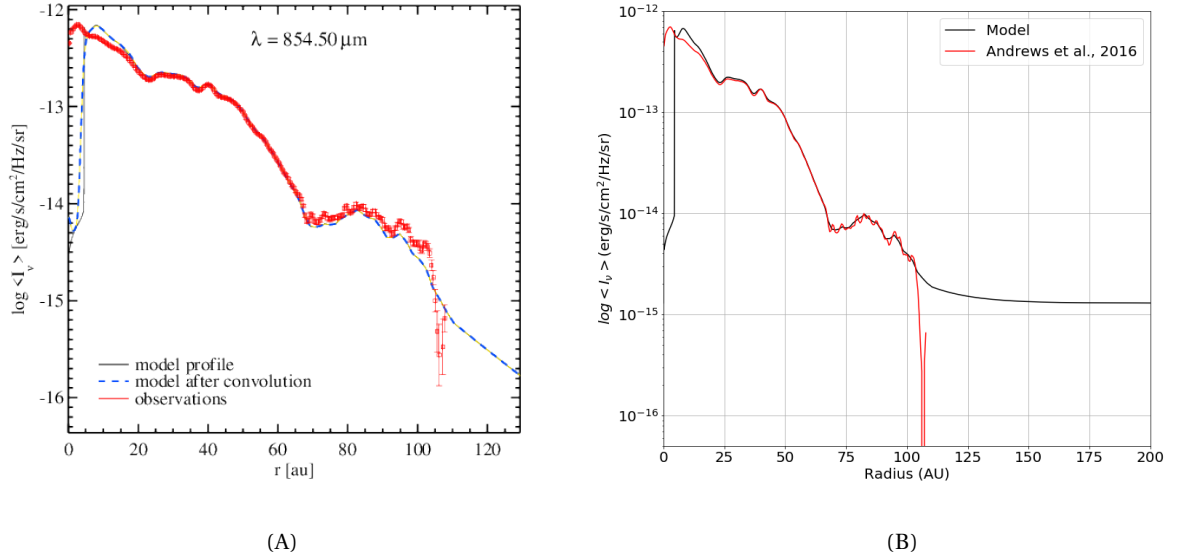


FIGURE 4.4: Output from the fifth run from the IDL script (4.4A) and the python script (4.4B) showing how the subtracted background in the IDL script influences the model profile.

this profile created by me. These two images are seen in Fig. 4.4. Figure 4.4A shows the output from the IDL script which comes with ProDiMo, Fig. 4.4B shows the output from the python script as created by me. The python script does not show the profile after the convolution with the ALMA beam. This convolution affects the inner disk mostly, which can be seen in Fig. 4.4A where the black profile only differs from the blue dashed profile in the first 10 AU, while for larger radii they are the same.

The surface brightness for $r > 60$ AU is the main region of interest in this section. From Fig. 4.4A it can be seen that, even though they are close, the surface brightness of the model is not matching the image data in this region. It can be seen that the substructure of the image profile is shown in the model profile, but the model profile is almost a factor two lower around 90 AU. Figure 4.4B shows the same profile from the same model versus the same image profile, but in this figure the image profile and the model profile match within 10 %. When looking at $f_{I/M}$ for this run, it can be seen that the maximum deviation from 1 is 27%.

Furthermore, for $r > 100$ AU Fig. 4.4A drops off to values below $10^{-16} \text{ erg/s/cm}^2/\text{Hz/sr}$, while the python script shows the profile heading to $10^{-15} \text{ erg/s/cm}^2/\text{Hz/sr}$ asymptotically. This difference in these profiles is created by the background of the images. The IDL script automatically removes the background of all the images it creates, therefore also in the surface brightness profiles. It assumes the background to be equal to the last value it calculates for the surface brightness, in this way forcing the surface brightness of the disk to have a value of zero at the edge. In these models, this value corresponds to $1.297 \times 10^{-15} \text{ erg/s/cm}^2/\text{Hz/sr}$. In comparison to the python profiles, which do not subtract the background, the behaviour of the outer region, after 125 AU, can be explained. If the python script is forced to subtract the background as well, the deviation of $f_{I/M}$ from 1 is found to be 80 %. This found background is not noise, but a combination of the interstellar radiation field including, for example, the cosmic microwave background. The model considers this background emission which is then picked up in the model images.

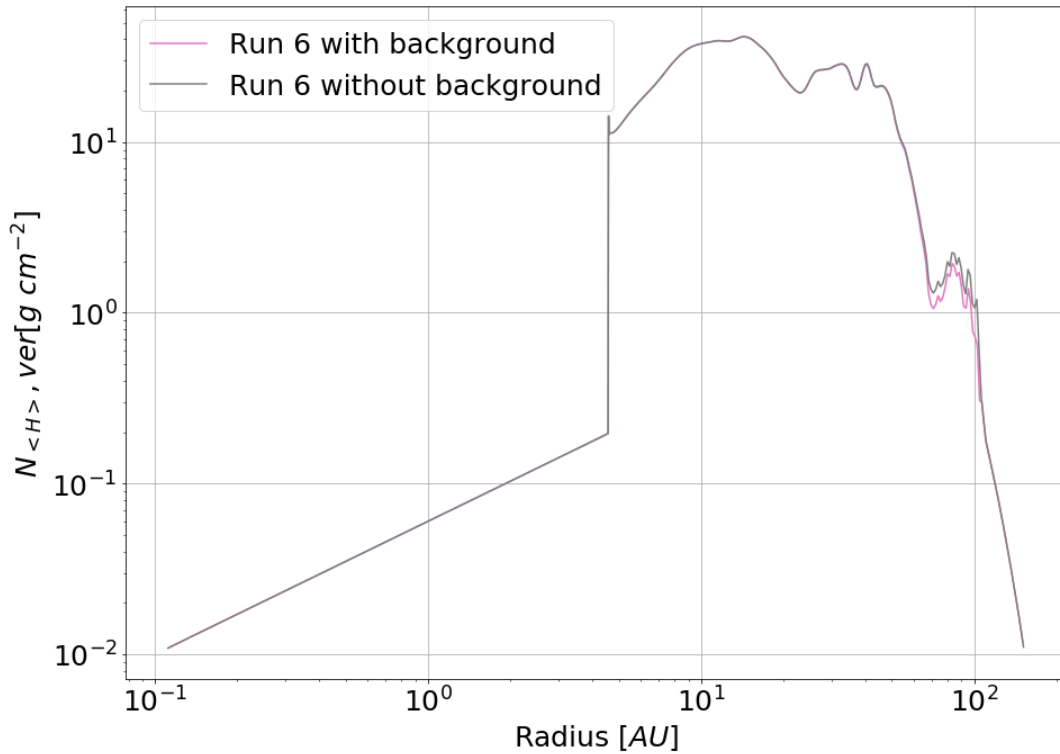


FIGURE 4.5: Comparison between the two different column densities for the sixth run with (pink) and without background (grey). The two profile appear to be equal up to ~ 60 AU, for larger radii the profile with background has a lower column density, as the background adds to the total surface brightness of the disk.

Currently it is not known if the ALMA observations could detect this, but the model suggest it could.

As the difference between the model surface brightness profile with background and the model surface brightness profile without background are noticeable by eye, the influence of this background will be further investigated. This fifth run will be rerun once with a factor $f_{I/M}$ as calculated between the image profile and the model profile with the background creating a column density which should be roughly equal to the current column density. The other run will be with a model profile with a subtracted background, creating a slightly different $f_{I/M}$ in the region $60 \leq r \leq 125$ AU, creating a different column density from the previously used column density. These new column densities are shown in Fig. 4.5, where the column densities are equal up to 60 AU. For radii larger than 60 AU the column density for the run with the subtracted background is higher with respect to the column density with the background. This is as expected knowing that the background was adding to the total surface brightness of the disk.

The output of these two runs is shown in Fig. 4.6 and Fig. 4.7. In these two figures the comparison between the output from the IDL script and from the python script is shown. Figure 4.6 shows the output of the run where the background is not subtracted, thus having a model profile in python which asymptotically reaches the value of 10^{-15} erg/s/cm²/Hz/sr. Figure 4.7 shows the output for the run where we have applied the same procedure of setting the last value of the surface brightness equal to the background value and subtracting this value from the entire profile. For this run the python profile shows the same behaviour as the IDL profile, with a model profile decreasing to zero after ~ 125 AU.

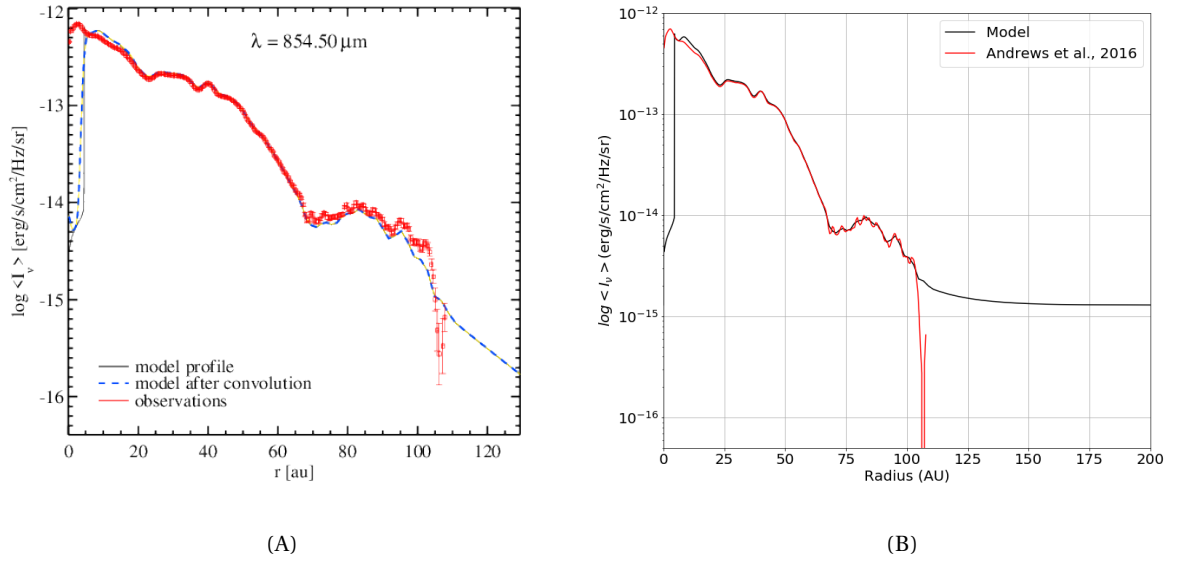


FIGURE 4.6: Output of the sixth run where the background is not subtracted. Figure 4.6A shows the IDL output of the model surface brightness profile (black) and the convolved surface brightness (blue dotted) versus the image profile. Figure 4.6B shows the the same profile but then in a python script. Note the difference between the two image profiles after ~ 60 AU.

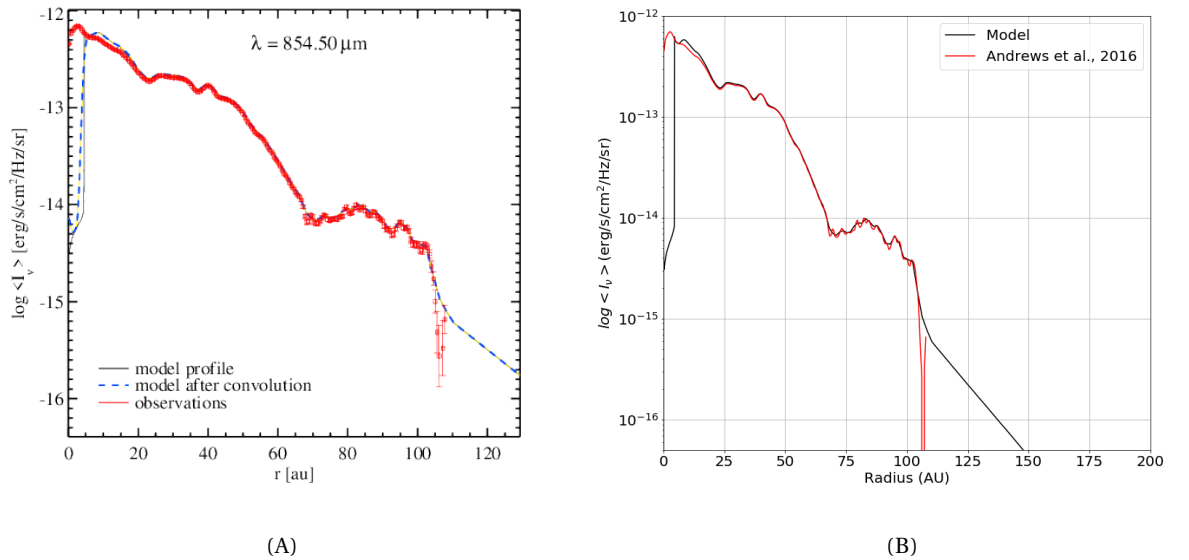


FIGURE 4.7: Output of the sixth run where the background is subtracted. Figure 4.7A shows the IDL output of the model surface brightness profile (black) and the convolved surface brightness (blue dotted) versus the image profile. Figure 4.7B shows the the same profile but then in a python script. Here the model profile is seen matching the image data in both of the determinations.

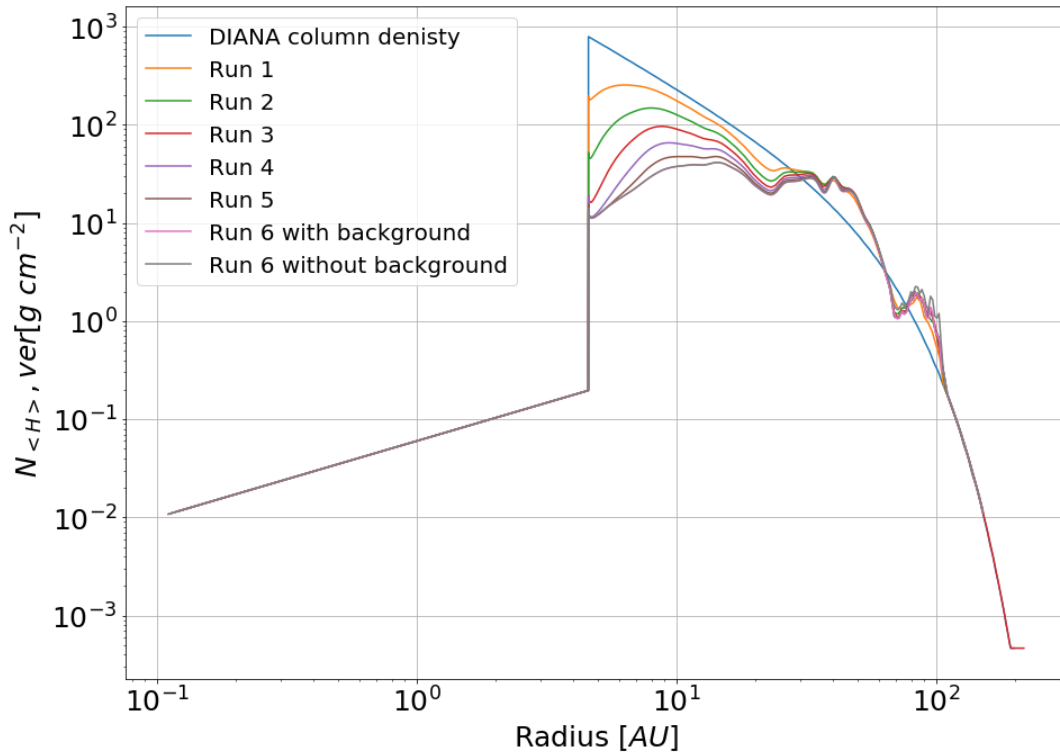


FIGURE 4.8: All the column densities of the different run versus the original DIANA column density (blue).

4.1.4 Final model

The sixth run will be the final run, as the column densities change in column density with respect to the previous column density was within 10%. Keeping in mind the uncertainties in the true value of the background and the resolution problems that came up during the different runs, a change of less than 10% is considered a good match. The model which has not subtracted the background is chosen as the final model for which a chemistry run will be started. For the previous run the choice was made to start from a known model, the DIANA model, to calculate the radiative transfer. For all of these runs the chemistry and disk gas temperatures were kept constant with respect to the DIANA model. The original DIANA model has a total disk mass of $0.0448 M_{\text{sun}}$, the final run of the model with adaptations has a mass of $0.02975 M_{\text{sun}}$. This is a total decrease of 34 percent of the disk mass. Figure 4.8 shows all of the column densities used for the different runs of the model with respect to the column density of the original DIANA model. Here it can be seen that the column density is decreased by a factor 100 in the region between 4.5 – 50 AU, explaining the decrease in disk mass. Even though this decrease seems massive, the outer regions show an increase in column density between 30 – 50 AU and 80 – 110 AU. As these increases happen at larger radii, the area over which this increase occurs is larger, adding more to the disk mass.

The output of the final model is shown in Fig. 4.9. Figure 4.9A shows the high resolution surface brightness profile with background of the model versus the image data by Andrews et al. (2016). Figure 4.9B shows the image representation of this surface brightness profile. If compared to the observed ALMA image (Fig. 1.1), it can be seen that the substructure in the disk is matching well.

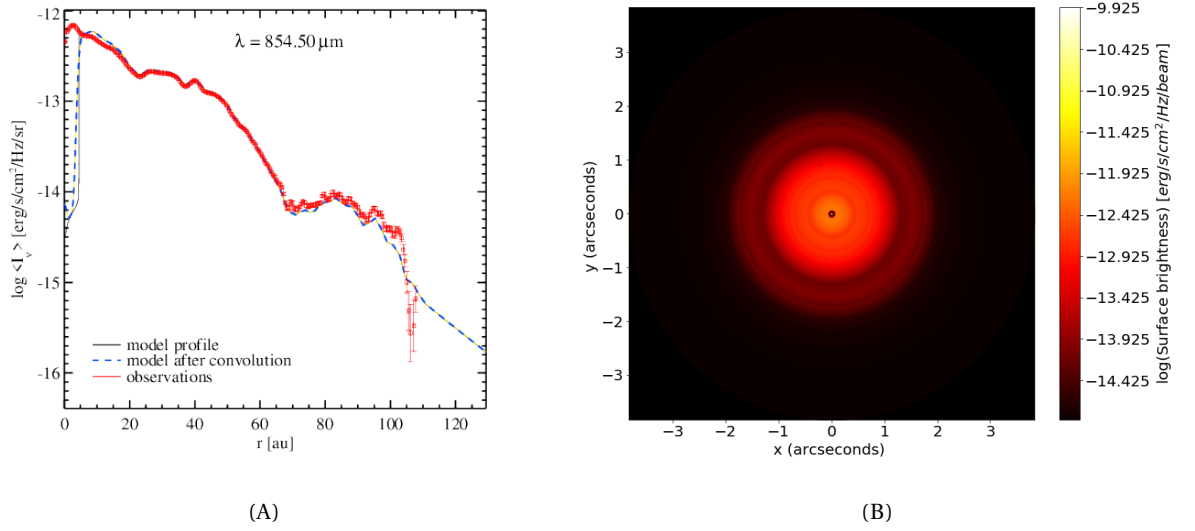


FIGURE 4.9: Output for the final run with adaptations. Figure 4.9A shows the image data by Andrews et al. (2016) (red) in comparison to the model surface brightness profile before (black) and after convolution with the ALMA beam (blue dashed). Figure 4.9B shows the image representation of this surface brightness profile.

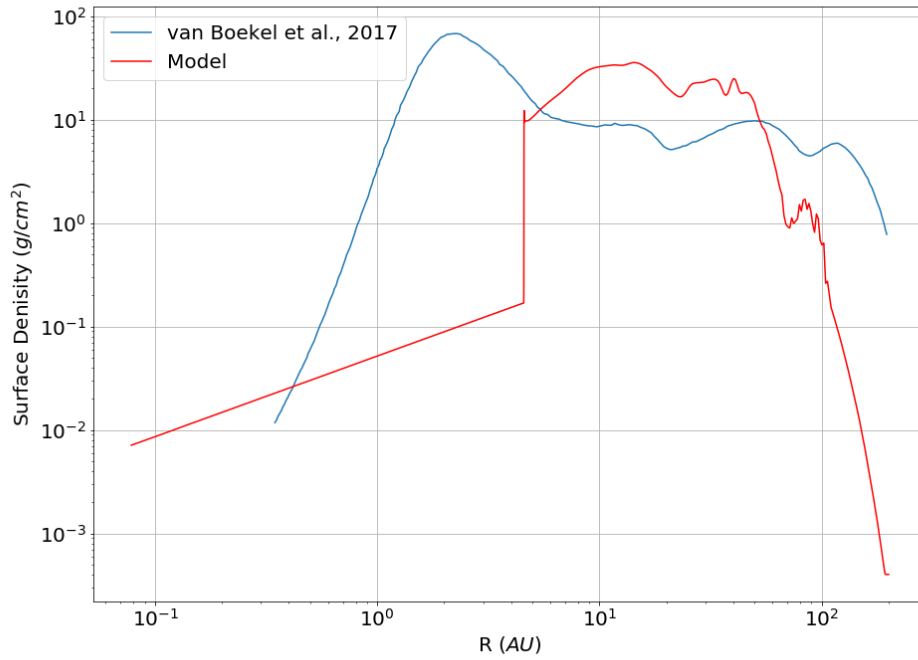


FIGURE 4.10: Comparison between the final model surface density profile (red) and the surface density of the gas by van Boekel et al. (2017).

4.2 Surface density

The surface density of the gas of the final model is compared to the surface density of the van Boekel et al. (2017) model constructed to match the SPHERE data. This comparison is shown in Fig. 4.10. From this figure it can be seen that the two profiles are roughly in the same order of magnitude, while still showing large deviations. In this thesis it was decided to ignore the modifications of the inner disk, hence the peak at ~ 3 AU can not be explained. From this figure it can also be seen that the peaks and dips corresponding to the van Boekel et al. (2017) do not match these in the DIANA model. Important to know is van Boekel et al. (2017) model the SPHERE data, while the DIANA model models the ALMA data. SPHERE traces the micron sized particles, while ALMA traces the larger mm sized particles. The difference between these two observations could cause the shift in the profiles. However, the dip at ~ 20 AU seems to occur in both profiles.

Figure 4.11 shows the comparison between the final DIANA model with adaptations and the van Boekel et al. (2017) model surface density of the large grains. By going through the procedure as described in Sect. 3.2 this profile is obtained, meaning we should see the surface density for the same grain population. van Boekel et al. (2017) do not specify if they model the full disk surface density or half of the disk surface density. As the latter is more common, from here on it will be assumed that they have modelled half the disk only. To correct for the different ranges of grain sizes the van Boekel et al. (2017) model is divided by 1.57, corresponding to the fraction of the grains with sizes modeled in the DIANA model to the 1-10 mm grain sizes from van Boekel et al. (2017). Figure 4.11 also shows how the surface density as determined by van Boekel et al. (2017) is almost 30 higher. However,

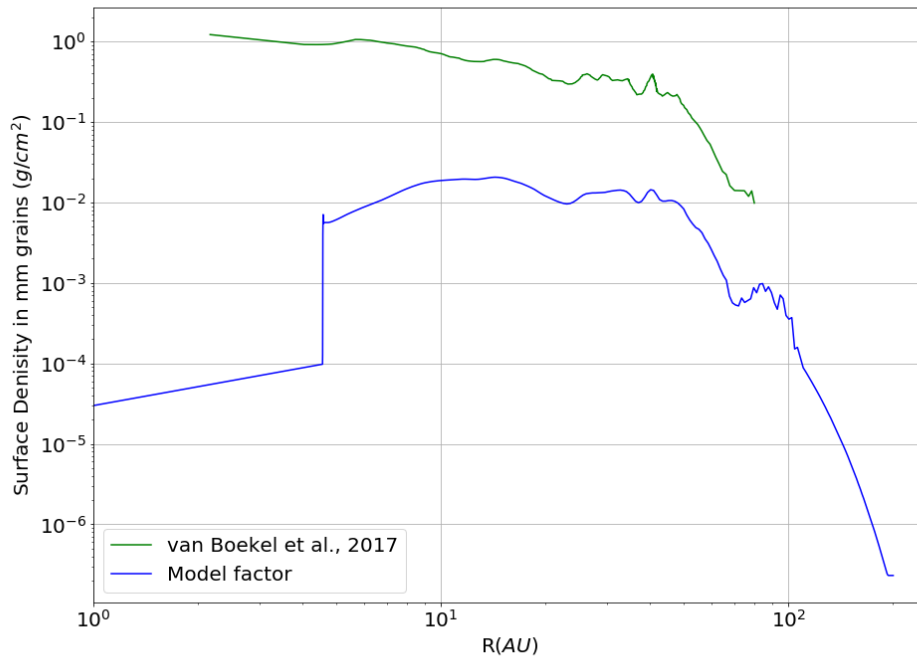


FIGURE 4.11: Comparison between the final model surface density profile of large grains (blue) and the surface density of large grains by van Boekel et al. (2017). These two profiles show a difference of a factor ~ 100 .

the smaller structures of this profile do show some similarities. For example, the large decrease at roughly 40 AU occurs in both of the profiles. Even the peak at 40 AU is visible in both profiles. The mean molecular weight assumed for this transformation was equal to 2.4 and corresponds to the mean molecular weight of the gas.

The difference between the profile by van Boekel et al. (2017) and the my final model turns out to be difficult to explain as the van Boekel et al. (2017) paper does not provide sufficient information on the initial assumptions made for their model. Also, it could be noted that their assumptions of large grains is quite extreme, as the DIANA model has a maximum grain size which is twice as small. The DIANA model used also photometry from the VLA (mm wavelength) to constrain the dust grain sizes. It is unclear whether the van Boekel et al. (2017) model has done the same. It is disturbing that both of these profiles, which should both match the high quality ALMA data, could come to such different results.

4.3 Chemistry

For the final model the chemistry calculation is turned back on. At first, the dust temperature, shown in Fig. 4.12, is compared to the dust temperature of the original DIANA model. In these figure the red dashed lines marked "1" and "10" denote the A_V extinction curves. As the photons penetrate the deepest where they encounter the least optical depth, the location of the lines can be defined as the minimum A_V in radial and vertical direction. This minimum is determined in the model by evaluating the column densities in the radial direction where the incident radiation originates from the star, and the vertical direction where the incident radiation originates from the interstellar medium. The A_V lines are determined by multiplying this column density with the dust opacity. Below the $A_V = 1$ line the disk gets optically thick, therefore no visible light radiates out from below this line and no visual radiation from the star or the interstellar radiation field can penetrate below this line. The $A_V = 1$ line in Fig. 4.12A extends up to $z/r = 0.125$ at 4.5 AU, which is the transition between the inner and outer disk. However, at the same radius in Fig. 4.12B this $A_V = 1$ extend up to $z/r = 0.09$, meaning that the disk in this region is getting less optically thick. From the comparison between the DIANA model and my final model it can be seen that the disk is less optically thick up to ~ 30 AU, after which the $A_V = 1$ line lies further from the midplane of the disk ($z/r = 0$). The exception to this higher $A_V = 1$ is found in one of the outer rings of the disk, located at ~ 75 AU, where the $A_V = 1$ line decreases by $z/r = 0.03$.

At 10 AU the DIANA model has a midplane dust temperature of 25 K, while the final model has a midplane dust temperature of 28 K. If the 40 K contour is inspected in these two plots, it can be seen that this contour is located at the same radius in the midplane (~ 6 AU), but at higher z/r this contour is more smooth in the final model. At 10 AU this 40 K contour is at $z/r = 0.12$ in the original DIANA model, while in the final model this line occurs at $z/r = 0.9$. The 20 K contour is pushed outwards, as the origin in the midplane of this contour in the DIANA model is at ~ 15 AU, while in the final model this origin comes closer to ~ 20 AU. In the previously discussed ring at ~ 75 AU the 20 K contour shows at dip, meaning that the dust temperature in this ring is slightly higher with respect to the surrounding region. From this it can be concluded that the overall dust temperature is increasing in the disk, even though the change is small. However, a small change can affect the chemistry and the dust emissivity.

Figure 4.13 shows the gas temperature of the two models, here again the dashed dotted line marked "1" and "10" denote the extinction lines in the visual. These lines are the same

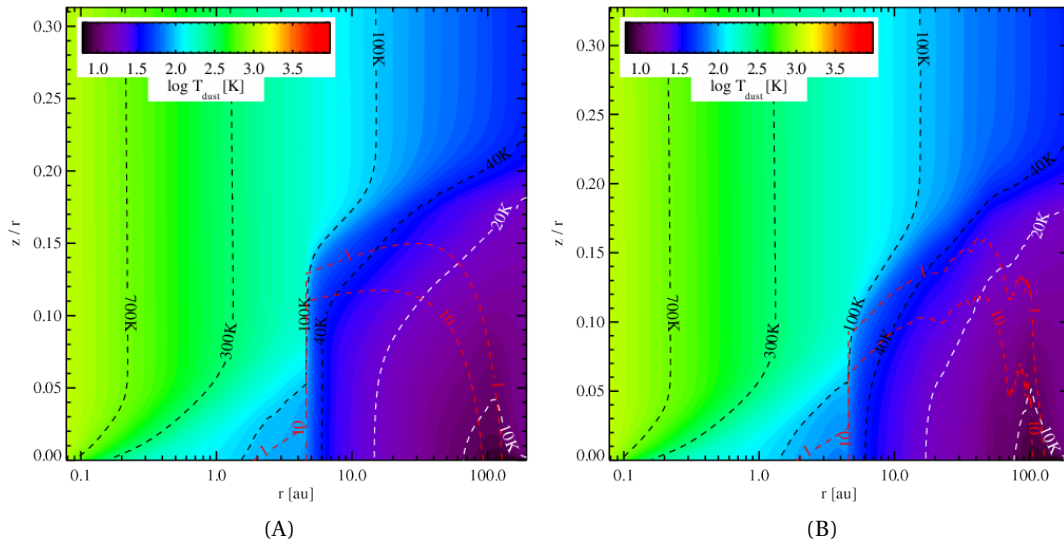


FIGURE 4.12: Dust temperature of the model. Figure 4.12A shows the dust temperature of the original DIANA model, Fig. 4.12B shows the dust temperature of the final model. The red lines marked "1" and "10" show the A_V lines

as shown in Fig. 4.12. The differences in the gas temperature with respect to the original DIANA model are less visible than those of the dust temperature. Here the 40 K contour originates from roughly the same radius in the midplane, and continues following roughly the same shape as in the original DIANA model. The 20 K contour is also not shifted in the midplane, but the peak of this contour, at 125 AU, has decreased in size with respect to the DIANA model. In the DIANA model this peak extends up to $z/r = 0.19$, while in the final model the maximum is found at $z/r = 0.18$.

Alongside the gas temperature versus the A_V lines the gas temperature is also shown versus the CO iceline. This CO iceline is shown in Fig. 4.14A and Fig. 4.14B as the red dashed line. What can be seen is that the curve of the final model is less steep as in the DIANA model. At 10 AU, the DIANA model CO iceline has a depth of $z/r = 0.11$, while the final model has a depth of $z/r = 0.07$. What can also be seen is that the maximum of this curve remains the same, in both the DIANA model and the final model the maximum of the CO iceline is at $z/r = 0.175$. The total CO ice mass in the original DIANA run is equal to $2.579 \times 10^{-6} M_{\text{sun}}$, the total CO ice mass of the final model is $2.664 \times 10^{-6} M_{\text{sun}}$. This is an increase of the total CO ice mass in the disk of $8.5 \times 10^{-8} M_{\text{sun}}$. As previously discussed, the value of the CO iceline has decreased, but still the total mass of the CO ice went up. The CO iceline shows a small increase with respect to the DIANA model between $\sim 40 - 60$ AU. Taking in mind the increase in the total CO ice mass, it can be concluded that the location of the CO ice is changing as the CO ice has moved towards the outer regions of the disk.

The following three figures show the line fluxes of three isotopologues of CO for the J=2 to J=1 transition; ^{12}CO (Fig. 4.15), ^{13}CO (Fig. 4.16) and C^{18}O (Fig. 4.17). The figures are subdivided into three frames, the top frame showing the optical depth of the line and the neighboring continuum as a function of radius. The middle frame showing the cumulative line flux in percents of the total line flux as function of radius. In the bottom frame the radial dashed lines are where 15 and 85 % radially originate. This is the same for the two vertical lines. That makes the box comprise $\sim 50\%$ of the emitted total line flux. The abundance of ^{13}CO to ^{12}CO is equal to $^{13}\text{CO}/^{12}\text{CO} = 0.014$, and the abundance of ^{16}O to ^{18}O is equal to 498.7 (Henkel, Whiteoak, and Mauersberger, 1994).

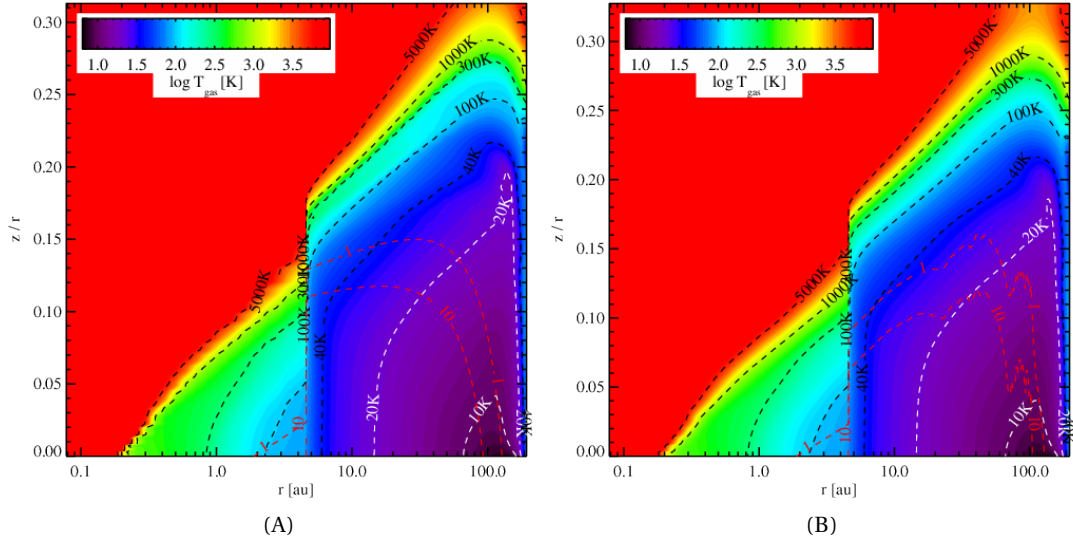


FIGURE 4.13: Gas temperature of the model. Figure 4.13A shows the gas temperature of the original DIANA model, Fig. 4.13B shows the gas temperature of the final model. The red lines marked "1" and "10" show the A_v lines

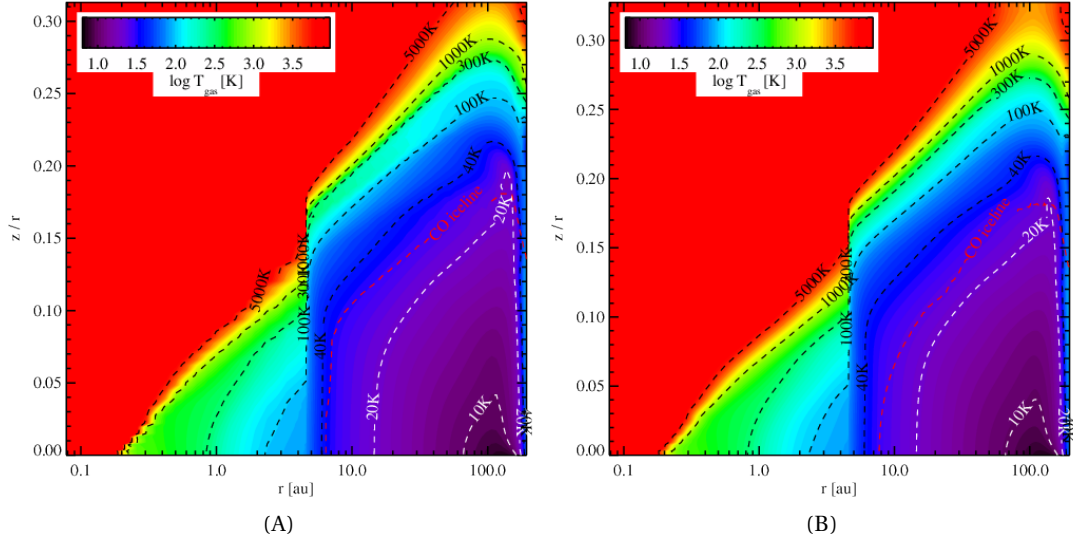


FIGURE 4.14: Gas temperature of the model. Figure 4.14A shows the gas temperature of the original DIANA model, Fig. 4.14B shows the gas temperature of the final model. The red dotted line shows the CO iceline below which the CO molecules are in the solid state.

If the top panel of the figures is compared for 4.15 it can be seen that in the final model the distribution of the flux is not as smooth as in the DIANA model, especially between 60 – 110 AU. The total line flux of the DIANA model is equal to $F_{\text{line}} = 1.61 \times 10^{-19} \text{W/m}^2$, while the total line flux of the final model is equal to $F_{\text{line}} = 1.73 \times 10^{-19} \text{W/m}^2$. This is an increase of $F_{\text{line}} = 0.12 \times 10^{-19} \text{W/m}^2$. The second panel does not differ much between the DIANA model and the final model. However, a small kink can be seen around ~ 100 AU.

The top panel of Fig. 4.16 shows roughly the same behaviour as in 4.15, where the substructure found in the surface brightness of the disk is showing between 60 – 100 AU. In the middle panel the cumulative flux is shown for the ^{13}CO isotopologue, which is

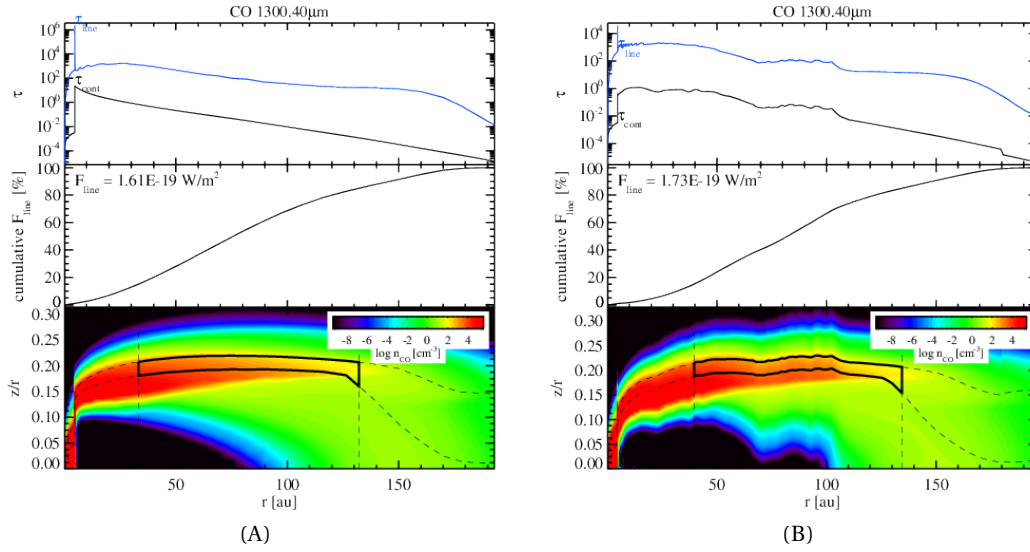


FIGURE 4.15: Fluxes for ^{12}CO , Fig. 4.15A shows the output from the original DIANA model, Fig. 4.15B shows the output from the model after the adaptations.

showing a clear kink at ~ 60 AU with respect to the original DIANA model. The DIANA model has a total line flux of $F_{\text{line}} = 2.77 \times 10^{-20} \text{ W/m}^2$ and my final model has a line flux of $F_{\text{line}} = 3.08 \times 10^{-20} \text{ W/m}^2$. This is again an increase in the total line flux, for ^{13}CO of $F_{\text{line}} = 0.31 \times 10^{-20} \text{ W/m}^2$.

The last isotopologue of interest is C^{18}O , shown in Fig. 4.17. For this isotopologue the optical depth in the top panel is showing the substructure created by the rings between 60 – 100 AU. The DIANA model has a total line flux of $F_{\text{line}} = 7.48 \times 10^{-21} \text{ W/m}^2$ and my final model has a line flux of $F_{\text{line}} = 8.84 \times 10^{-21} \text{ W/m}^2$. The line flux for C^{18}O has thus increased by $F_{\text{line}} = 1.36 \times 10^{-21} \text{ W/m}^2$.

As we process through these different isotopologues and compare the bottom panels, it can be seen that the rarer the isotopologue, the deeper the emission of this isotopologue originates in the disk. We have already concluded that the CO stays longer in the ice phase in final model, meaning there is less emission in this region. If the bottom panels are compared for each isotopologue, it can be seen that the highlighted black region shifts towards the midplane. For ^{12}CO (Fig. 4.15), the lower left corner is located at $z/r = 0.13$ for both models, for ^{13}CO (Fig. 4.16) this lower left corner appears at $z/r = 0.015$, and for C^{18}O (Fig. 4.17) the lower left corner is located at $z/r = 0.17$.

Overall it can be concluded that the substructure of the disk is indeed influencing the gas in the disk. The disk with substructure is warmer. The lines corresponding to the isotopologues of CO are changed with respect to the original DIANA model. argue that for the J=2-1 line ALMA has a noise of 0.008 Jy/beam , converted to $\text{W/m}^2/\text{Hz/beam}$, this result in a noise level which could be observed of $8 \times 10^{-29} \text{ W/m}^2/\text{Hz/beam}$. As the minimum change in line fluxes between the original model and the DIANA model is $F_{\text{line}} = 1.36 \times 10^{-21} \text{ W/m}^2$, these variations should be detectable by ALMA.

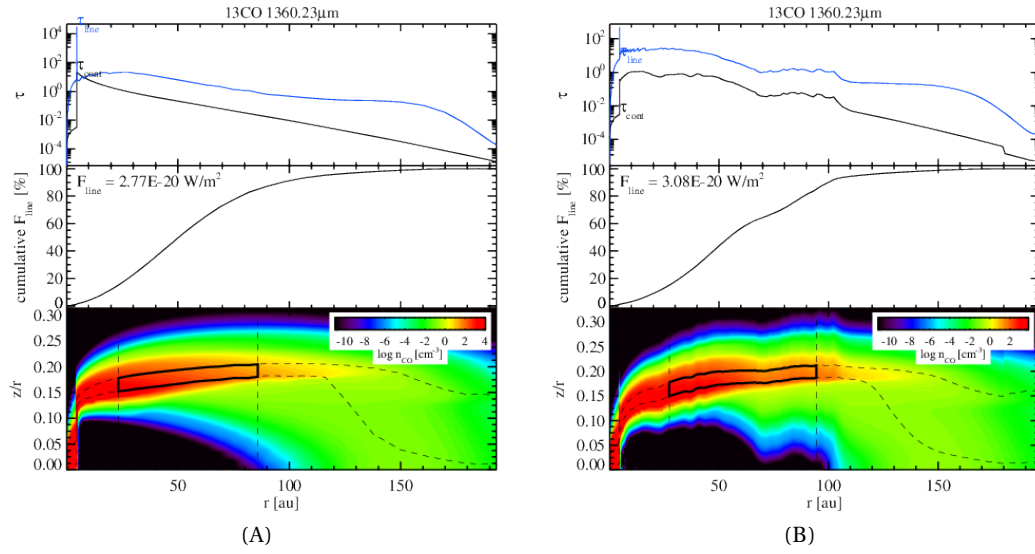


FIGURE 4.16: Fluxes for 13CO, Fig. 4.16A shows the output from the original DIANA model, Fig. 4.16B shows the output from the model after the adaptations

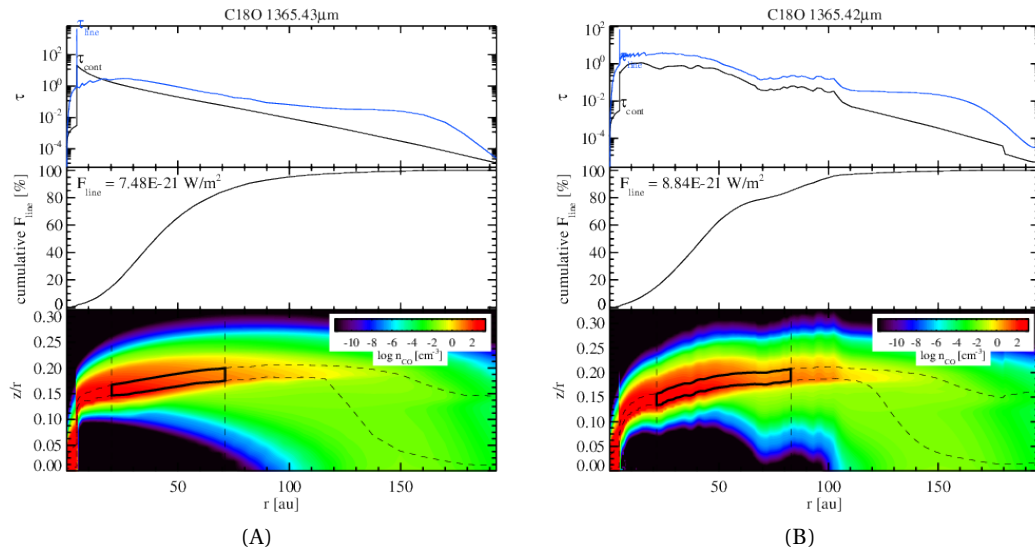


FIGURE 4.17: Fluxes for C18O, Fig. 4.17A shows the output from the original DIANA model, Fig. 4.17B shows the output from the model after the adaptations

Chapter 5

Discussion

During the course of this thesis a number of issues came up. First of all, ProDiMo was not prepared for an observational data set with such a high resolution. While progressing through the thesis the need for an even higher resolution profile came up, which has added quite a lot in computational time. Dependent on the usage of the different machines available at the Kapteyn Institute, the run time of a model could vary from 6 - 24 hours in real time. This makes it rather difficult to go through many model calculations.

Another point of discussion is the determination of the background surface brightness for the models. The IDL script used in the analysis subtracts a background value from the model image. The background value in this case is defined as the value for the surface brightness at the outermost radial point. Normally this would not make that much of a difference, but for the case of TW Hya this difference turns out to be almost a factor 2 in the region between 60 and 110 AU. At this high spatial resolution ALMA will filter out large scale emission because it is an interferometer - high spatial resolution imaging will also significantly limit the largest detectable scales and any emission larger than those scales will be filtered out. This aspect is not properly included in the model since the model only does a beam convolution. Interesting would be to investigate if this background is really observable with ALMA and how significant the effect of that is on the overall surface brightness of the TW Hya disk.

After the final model was reached which matched the surface brightness of the observations within 10 % the comparison was made with an earlier model of the TW Hya disk by van Boekel et al. (2017). Here it was discovered that it was rather hard to compare the surface densities of van Boekel et al. (2017) of the large grains to the surface density of the large grains in the model used in this thesis. There are quite some differences between the DIANA model and the van Boekel et al. (2017) model. First, they have used an MRN grain size distribution which was not continuous between the smallest and largest of the grain sizes. The DIANA model uses a power for the grain size distribution equal to ~ 4 . After trying a number of corrections such as accounting for the same minimum/maximum grain sizes, the difference in gas-to-dust mass ratio, the difference between the two surface densities was still a factor 50. After carefully reading their paper we concluded that their ALMA model was hard to understand as they do not provide sufficient information of the details and assumptions in this model. In general, getting a disk structure model that fits SPHERE and ALMA. However, it is quite disturbing to see the large discrepancies when comparing two models who claim to fit the same data. For further research on this difference the detailed model structure and input files of van Boekel et al. (2017) should be compared to the model structure of the final model of this thesis in order to get a more in depth view of the differences between these two models.

Chapter 6

Conclusion

In this thesis the aim was to adapt an existing model for the T Tauri star TW Hya to match the recent high spatial resolution observations by ALMA. The original model from the DIANA project did not show any substructure in the surface brightness as it matched earlier low resolution ALMA data which does not show any substructure. The new ALMA observation by Andrews et al. (2016) show a ringed substructure in the protoplanetary disk of TW Hya.

The initial model was adapted to match the observations with rings in the following way; at first the model profile was divided by the image profile, creating a factor called $f_{I/M}$. The current column density is multiplied by $f_{I/M}$ to create a new column density which was used as the input column density for the follow up run. What was immediately noticed is that the image profile by Andrews et al. (2016) extends out to only 125 AU, while the model calculates the surface brightness out to 200 AU. We accounted for this by creating a new factor for the adaptations which was a combination of a weighted image profile and an extrapolated image profile.

After three runs it could be seen that some of the substructure of the image profile was not showing up in the model profile, as the model resolution was not high enough to capture the substructure. This gave rise to a new higher resolution model with almost double the data points. Two more runs were done with this high resolution model, after which it was concluded that there exists a difference between the figures created with the corresponding IDL script and my images using ProDiMopy and python. This difference originates in the value of the background in the images. The IDL script automatically subtracts the background value, calculated as the last value in the surface brightness profile, while the python script does not. The background value is 1.297×10^{-15} erg/s/cm²/Hz/sr. The run after this run is calculated twice; once with the background as was done in the runs before, once without the background to investigate to which extend the surface brightness is influenced by this background. The true value of the model profile, either with or without background, is difficult to determine as the large scale background is filtered out in interferometric observations.

This final run was also compared to another disk model of TW Hya by van Boekel et al. (2017) where they have modeled SPHERE observations. What could be concluded here was that the gas surface density was within the same order of magnitude with respect to the original DIANA model, however the substructure of these two profiles was shifted radially with respect to each other. This shift could originate from the comparison between the SPHERE and ALMA data. The surface density of the large grains is also investigated and turned out to be a factor ~ 30 higher. The recreation of the profile of van Boekel et al. (2017) turns out to be rather difficult as their paper does not specify all conditions and parameters that were used to create the TW Hya model.

Upon comparing the chemistry of the final run and the original DIANA model it could be concluded that the dust temperature of the final run is higher by ~ 3 K at 10 AU. It was also concluded that the total CO ice mass went up by $8.5 \times 10^{-8} M_{\text{sun}}$ and that the location of the CO ice shifted towards the outer edge of the disk. The line fluxes of ^{12}CO show an increase of $0.12 \times 10^{-19} \text{ W/m}^2$ with respect to the DIANA model. The increase for ^{13}CO and C^{18}O are $0.31 \times 10^{-20} \text{ W/m}^2$ and $1.36 \times 10^{-21} \text{ W/m}^2$ respectively. argue that for the J=2-1 line ALMA has a noise of 0.008 Jy/beam, converted to $\text{W/m}^2/\text{Hz}/\text{beam}$, this result in a noise level which could be observed of $8 \times 10^{-29} \text{ W/m}^2/\text{Hz}/\text{beam}$. As the minimum change in line fluxes between the original model and the DIANA model is $F_{\text{line}} = 1.36 \times 10^{-21} \text{ W/m}^2$, these variations should be detectable by ALMA.

The original DIANA model has a total disk mass of $0.0448 M_{\text{sun}}$, the final run of the model with adaptations has a mass of $0.02975 M_{\text{sun}}$. This is a total decrease of 34 % of the disk mass.

Bibliography

In:

- Alexander, R. et al. (2014). “The Dispersal of Protoplanetary Disks”. In: *Protostars and Planets VI*. Ed. by Henrik Beuther et al., p. 475. DOI: [10.2458/azu_uapress_9780816531240-ch021](#). arXiv: [1311.1819 \[astro-ph.EP\]](#).
- Andrews, S. M. et al. (2012). “The TW Hya Disk at 870 μm : Comparison of CO and Dust Radial Structures”. In: *Astrophysical Journal* 744, 162, p. 162. DOI: [10.1088/0004-637X/744/2/162](#). arXiv: [1111.5037 \[astro-ph.EP\]](#).
- Andrews, S. M. et al. (2016). “Ringed Substructure and a Gap at 1 au in the Nearest Protoplanetary Disk”. In: *Astrophysical Journal, Letters* 820, L40, p. L40. DOI: [10.3847/2041-8205/820/2/L40](#). arXiv: [1603.09352 \[astro-ph.EP\]](#).
- Appenzeller, I. and R. Mundt (1989). “T Tauri stars”. In: *Astronomy and Astrophysics Review* 1, pp. 291–334. DOI: [10.1007/BF00873081](#).
- Bae, Jaehan, Zhaohuan Zhu, and Lee Hartmann (2017). “On the Formation of Multiple Concentric Rings and Gaps in Protoplanetary Disks”. In: *Astrophysical Journal* 850, 201, p. 201. DOI: [10.3847/1538-4357/aa9705](#). arXiv: [1706.03066 \[astro-ph.EP\]](#).
- Bergin, Edwin A. et al. (2013). “An old disk still capable of forming a planetary system”. In: *Nature* 493, pp. 644–646. DOI: [10.1038/nature11805](#). arXiv: [1303.1107 \[astro-ph.SR\]](#).
- Blum, Jürgen et al. (2006). “The Physics of Protoplanetary Dust Agglomerates. I. Mechanical Properties and Relations to Primitive Bodies in the Solar System”. In: *Astrophysical Journal* 652, pp. 1768–1781. DOI: [10.1086/508017](#).
- Carmona, A. et al. (2014). “Constraining the structure of the transition disk HD 135344B (SAO 206462) by simultaneous modeling of multiwavelength gas and dust observations”. In: *Astronomy and Astrophysics* 567, A51, A51. DOI: [10.1051/0004-6361/201322534](#). arXiv: [1403.6193 \[astro-ph.SR\]](#).
- Debes, John H. et al. (2013). “The 0.5–2.22 μm Scattered Light Spectrum of the Disk around TW Hya: Detection of a Partially Filled Disk Gap at 80 AU”. In: *Astrophysical Journal* 771, 45, p. 45. DOI: [10.1088/0004-637X/771/1/45](#). arXiv: [1306.2969 \[astro-ph.EP\]](#).
- Dong, Ruobing et al. (2017). “Multiple Disk Gaps and Rings Generated by a Single Super-Earth”. In: *Astrophysical Journal* 843, 127, p. 127. DOI: [10.3847/1538-4357/aa72f2](#). arXiv: [1705.04687 \[astro-ph.EP\]](#).
- Draine, B. T. (2011). *Physics of the Interstellar and Intergalactic Medium*.
- Duffell, Paul C. (2015). “A Simple Analytical Model for Gaps in Protoplanetary Disks”. In: *Astrophysical Journal* 807, L11, p. L11. DOI: [10.1088/2041-8205/807/1/L11](#). arXiv: [1505.03514 \[astro-ph.EP\]](#).
- Haisch Karl E., Jr., Elizabeth A. Lada, and Charles J. Lada (2001). “Disk Frequencies and Lifetimes in Young Clusters”. In: *Astrophysical Journal* 553, pp. L153–L156. DOI: [10.1086/320685](#). arXiv: [astro-ph/0104347 \[astro-ph\]](#).
- Hein Bertelsen, R. P. et al. (2014). “CO ro-vibrational lines in HD 100546. A search for disc asymmetries and the role of fluorescence”. In: *Astronomy and Astrophysics* 561, A102, A102. DOI: [10.1051/0004-6361/201322574](#). arXiv: [1311.5353 \[astro-ph.GA\]](#).
- Henkel, C., J. B. Whiteoak, and R. Mauersberger (1994). “Dense gas in nearby galaxies. VII. The active nucleus of NGC 4945.” In: *Astronomy and Astrophysics* 284, pp. 17–27.

- Isella, Andrea and Neal J. Turner (2018). “Signatures of Young Planets in the Continuum Emission from Protostellar Disks”. In: *Astrophysical Journal* 860, 27, p. 27. DOI: [10.3847/1538-4357/aabb07](#).
- Kamp, I. and C. P. Dullemond (2004). “The Gas Temperature in the Surface Layers of Protoplanetary Disks”. In: *Astrophysical Journal* 615, pp. 991–999. DOI: [10.1086/424703](#). arXiv: [astro-ph/0408501](#) [astro-ph].
- Kamp, I. and G. J. van Zadelhoff (2001). “On the gas temperature in circumstellar disks around A stars”. In: *Astronomy and Astrophysics* 373, pp. 641–656. DOI: [10.1051/0004-6361:20010629](#). arXiv: [astro-ph/0105300](#) [astro-ph].
- Kamp, Inga and Frank Bertoldi (2000). “CO in the circumstellar disks of Vega and beta Pictoris”. In: *Astronomy and Astrophysics* 353, pp. 276–286.
- Maciel, Walter J. (2013). *Astrophysics of the Interstellar Medium*. DOI: [10.1007/978-1-4614-3767-3](#).
- Mayor, Michel and Didier Queloz (1995). “A Jupiter-mass companion to a solar-type star”. In: *Nature* 378, pp. 355–359. DOI: [10.1038/378355a0](#).
- Menu, J. et al. (2014). “On the structure of the transition disk around TW Hydrae”. In: *Astronomy and Astrophysics* 564, A93, A93. DOI: [10.1051/0004-6361/201322961](#). arXiv: [1402.6597](#) [astro-ph.SR].
- Min, M. et al. (2009). “Radiative transfer in very optically thick circumstellar disks”. In: *Astronomy and Astrophysics* 497, pp. 155–166. DOI: [10.1051/0004-6361/200811470](#). arXiv: [0902.3092](#) [astro-ph.IM].
- Muro-Arena, G. A. et al. (2018). “Dust modeling of the combined ALMA and SPHERE datasets of HD 163296. Is HD 163296 really a Meeus group II disk?” In: *Astronomy and Astrophysics* 614, A24, A24. DOI: [10.1051/0004-6361/201732299](#). arXiv: [1802.03328](#) [astro-ph.EP].
- Pinte, C. et al. (2006). “Monte Carlo radiative transfer in protoplanetary disks”. In: *Astronomy and Astrophysics* 459, pp. 797–804. DOI: [10.1051/0004-6361:20053275](#). arXiv: [astro-ph/0606550](#) [astro-ph].
- Qi, C. et al. (2013). “Imaging of the CO Snow Line in a Solar Nebula Analog”. In: *Science* 341, pp. 630–632. DOI: [10.1126/science.1239560](#). arXiv: [1307.7439](#) [astro-ph.SR].
- Setiawan, J. et al. (2008). “A young massive planet in a star-disk system”. In: *Nature* 451, pp. 38–41. DOI: [10.1038/nature06426](#).
- Shu, F. H. (1977). “Self-similar collapse of isothermal spheres and star formation”. In: *Astrophysical Journal* 214, pp. 488–497. DOI: [10.1086/155274](#).
- Torres, C. A. O. et al. (2006). “Search for associations containing young stars (SACY). I. Sample and searching method”. In: *Astronomy and Astrophysics* 460, pp. 695–708. DOI: [10.1051/0004-6361:20065602](#). arXiv: [astro-ph/0609258](#) [astro-ph].
- van Boekel, R. et al. (2017). “Three Radial Gaps in the Disk of TW Hydrae Imaged with SPHERE”. In: *Astrophysical Journal* 837, 132, p. 132. DOI: [10.3847/1538-4357/aa5d68](#). arXiv: [1610.08939](#) [astro-ph.EP].
- Williams, Jonathan P. and Lucas A. Cieza (2011). “Protoplanetary Disks and Their Evolution”. In: *Annual Review of Astronomy and Astrophysics* 49, pp. 67–117. DOI: [10.1146/annurev-astro-081710-102548](#). arXiv: [1103.0556](#) [astro-ph.GA].
- Woitke, P., I. Kamp, and W. F. Thi (2009). “Radiation thermo-chemical models of protoplanetary disks. I. Hydrostatic disk structure and inner rim”. In: *Astronomy and Astrophysics* 501, pp. 383–406. DOI: [10.1051/0004-6361/200911821](#). arXiv: [0904.0334](#) [astro-ph.EP].
- Woitke, P. et al. (2018a). “Consistent dust and gas models for protoplanetary disks III. Models for selected objects from the FP7 DIANA project”. In: *arXiv e-prints*, arXiv:1812.02741, arXiv:1812.02741. arXiv: [1812.02741](#) [astro-ph.EP].

- Woitke, P. et al. (2018b). “Modelling mid-infrared molecular emission lines from T Tauri stars.” In: *Astronomy and Astrophysics* 618A, pp. 57–57. arXiv: [1807.05784 \[astro-ph.SR\]](#).
- Zhang, Shangjia et al. (2018). “The Disk Substructures at High Angular Resolution Project (DSHARP). VII. The PlanetDisk Interactions Interpretation”. In: *Astrophysical Journal* 869, L47, p. L47. DOI: [10.3847/2041-8213/aaf744](#). arXiv: [1812.04045 \[astro-ph.EP\]](#).